

Probabilistic Shaping Distributions for Optical Communications

Ethan M. Liang , *Graduate Student Member, IEEE*, and Joseph M. Kahn , *Life Fellow, IEEE*

(Invited Tutorial)

Abstract—Probabilistic shaping is widely employed in local oscillator-based coherent optical systems to improve receiver sensitivity and provide rate adaptation. This widespread adoption has been enabled, in part, by simple closed-form solutions for the optimal input distribution and channel capacity for these standard coherent channels. By contrast, the optimal input distributions and channel capacities for many direct-detection optical channels remain open problems. The lack of non-negative root-Nyquist pulses, signal-dependent noise, and the possible discreteness of the capacity-achieving input distribution have historically prevented standard information-theoretic techniques from obtaining simple closed-form solutions for these channels. In this tutorial, we review a high-rate continuous approximation (HCA) for analytically approximating the optimal input distribution. HCA, which was first developed for source coding, approximates the input constellation by a dense high-dimensional coset code that can be approximated well by a continuum, transforming the problem of computing the optimal input distribution subject to an average-power constraint to a problem of finding a minimum-energy shaping region in a high-dimensional continuous space. HCA yields closed-form continuous approximations to the capacity-achieving input distributions and shaping gains at high signal-to-noise ratio. We explain how enumerating a coset code in natural coordinates enables extension of HCA to direct-detection optical channels, allowing one to obtain closed-form approximations for the capacity-achieving input distributions and shaping gains for a variety of direct-detection systems that detect the intensity or Stokes vector and are limited by thermal or optical amplifier noise. We also discuss the implementation of probabilistic shaping in direct-detection systems.

Index Terms—Direct detection, fiber optic communication, probabilistic shaping, stokes vector receiver.

I. INTRODUCTION

PROBABILISTIC shaping for channels using coherent detection with additive Gaussian noise has been studied extensively since Shannon derived the optimal input distribution and capacity for these standard coherent (SC) channels [1].

Received 15 July 2024; revised 20 November 2024; accepted 26 December 2024. Date of publication 14 January 2025; date of current version 17 February 2025. This work was supported in part by Meta through the Stanford Photonics Research Center, in part by the Stanford System X Alliance, and in part by the National Science Foundation under Grant DGE-1656518. (Corresponding author: Ethan M. Liang.)

The authors are with the E. L. Ginzton Laboratory, Department of Electrical Engineering, Stanford University, Stanford, CA 94305 USA (e-mail: emliang@stanford.edu; jmk@ee.stanford.edu).

Color versions of one or more figures in this article are available at <https://doi.org/10.1109/JLT.2025.3528835>.

Digital Object Identifier 10.1109/JLT.2025.3528835

Much of the work on probabilistic shaping for SC channels can be categorized into one of two areas: 1) algorithmic methods for achieving a target discrete-valued input distribution or 2) analytical and numerical methods for computing optimal continuous- or discrete-valued input distributions and the resulting channel capacities under various constraints.

A key advance in the algorithmic implementation of probabilistic shaping was the probabilistic amplitude shaping (PAS) architecture [2]. PAS provides a flexible framework in which a fixed distribution matcher (DM) can be combined with an independently designed forward error-correction (FEC) code to achieve a target discrete input distribution. This architecture was first demonstrated using a constant-composition DM (CCDM) [3], but alternative schemes yielding superior performance at finite block lengths have also been developed [4]. Work on algorithmic approaches that do not use PAS is summarized in [5].

On the analytical front, since Shannon's seminal work, substantial progress has been made in obtaining closed-form solutions for the optimal input distributions and capacities of various electrical channels using coherent detection. Examples of channels studied include statistically parameterized wireless channels [6], multi-input multi-output channels [7], [8], and multi-user channels [9], [10]. On the numerical front, methods for computing the capacity-achieving input distribution were pioneered in [11], [12].

Local oscillator (LO)-based coherent optical systems are well-modeled as SC channels, and have extensively employed the aforementioned theories and algorithms, most of which were first developed for electrical channels. (A notable exception is the PAS architecture [2], which was first motivated, in part, by applications in coherent optical systems [5].)

By contrast, the capacities and capacity-achieving input distributions for several important direct-detection (DD) optical methods remain open problems. The most common DD scheme simply uses a photodetector to detect an intensity-modulated signal. We refer to this method as standard direct (SD) detection (it is often called intensity modulation/direct detection, IM/DD). Closed-form solutions for the capacity and capacity-achieving input distributions for SD optical channels are not known [13], [14], although tight lower and upper bounds for the capacity under average power constraints [15], [16] or peak and average power constraints [17], [18], [19] have been derived. There has also been substantial progress in deriving properties of

the capacity-achieving input distribution under various channel constraints. The capacity-achieving input distribution under peak and average power constraints was proven to be both discrete and finite [20], and an algorithm to numerically compute the capacity-achieving input distribution has been given [14]. The capacity-achieving input distribution for average power-constrained SD channels with signal-dependent Gaussian noise has been shown to be discrete with a countably infinite support set [14], [21]. While the form of the capacity-achieving input distribution for average power-constrained SD channels with only signal-independent Gaussian noise is not known, the best schemes to date used finite, discrete input distributions [16].

Beyond simple SD detection, Stokes vector (SV) detection [22], [23], [24] and Kramers Kronig (KK) detection [25] are alternative DD-based methods that are actively studied for possible use in next-generation short-reach optical links. These methods provide higher signal dimensionalities than traditional SD detection, enabling scaling up of per-wavelength data rates without necessarily increasing the symbol rate. Previous work on the optimal input distributions and capacities of these methods included study of thermal noise-limited SV detection under constraints on detected electrical power [24], amplifier noise-limited SV detection under constraints on detected electrical power [26], and amplifier noise-limited KK detection in the high carrier-to-signal power ratio regime [27]. While we would like to derive closed-form analytic solutions for the capacity-achieving input distributions and capacities for SD, SV, and KK detection in the thermal noise-limited and amplifier noise-limited regimes, these remain open problems. In the absence of exact solutions, it is desirable to have a framework in which to derive approximate capacity-achieving input distributions for these receivers, at least at high signal-to-noise ratios (SNRs).

In this tutorial paper, we review the high-rate continuous approximation (HCA) and its application to DD optical methods. HCA was originally developed to analytically estimate the distortion in scalar [28] and vector source coding [29], [30] in the high-resolution regime. HCA was later extended by G. D. Forney and L.-F. Wei to channel coding for SC channels [31]. In this paper, we use HCA to compute closed-form analytic approximations to the capacity-achieving input distribution at high SNR.¹ In the context of capacity-approaching high-dimensional lattice codes, HCA approximates the input constellation as a continuum contained within a geometric shaping region. HCA reduces the problem of probabilistic shaping to determination of the minimum-energy shaping region in a high-dimensional continuous geometric space. The distribution induced in the basic signaling dimensions and the shaping gain become properties of the minimum-energy shaping region. HCA was subsequently applied to thermal noise-limited SD detection [32], [33], amplifier noise-limited SD detection [34], and SV detection in the thermal noise-limited and amplifier noise-limited regimes [35],

¹In this paper, we neglect memory effects in all channels, which may arise from uncompensated channel dispersion or transmit pulses that are not orthogonal to time translates by all nonzero integer multiples of the symbol period (see Section II-B). In a channel with memory, our analysis approximates the optimal input distribution for a memoryless channel with the same marginal statistics as the actual channel.

yielding closed-form analytical approximations for the optimal input distribution and shaping gain for each method.

There are several previous tutorial and review papers covering various aspects of probabilistic shaping for optical communications. PAS and CCDM with a focus on algorithmic implementation are presented in [5]. Another tutorial paper on PAS and CCDM with a comprehensive presentation of relevant information-theoretic concepts and metrics is presented in [36]. An alternative DM approach using enumerative sphere shaping is presented in [4]. A tutorial on practical hardware implementation of probabilistic shaping is presented in [37]. Numerical computation of the optimal input distribution of the thermal noise-limited SD receiver under peak-power constraints is presented in [38]. Comprehensive overviews of capacity results for the SD receiver are presented in [13], [14].

By contrast, this tutorial paper focuses on deriving closed-form continuous approximations to the capacity-achieving input distributions and shaping gains at high SNR for a variety of DD-based methods, which detect different physical variables, including optical intensity, SV, and optical electric field, in both the thermal noise-limited and amplifier noise-limited regimes. This paper studies a total of six different discrete-time channel models, each resulting in a different input distribution.

The remainder of this paper is structured as follows. In Section II, we distinguish between LO-based and direct detection, provide an overview of the DD methods covered in this tutorial, and list our assumptions and performance metrics. In Section III, we briefly cover Shannon's derivation of the SC detection channel capacity before presenting an overview of HCA. We then apply HCA to SC detection and show that the results exactly match those obtained by Shannon. In Section IV, we introduce the concept of natural coordinates, allowing us to extend HCA to DD-based methods. We then use HCA to derive continuous approximations to the optimal input distribution and shaping gain for the SD detection and SV detection in the thermal noise-limited and amplifier noise-limited regimes. We also consider probabilistic shaping for KK detection in the amplifier noise-limited regime. In Section V, we discuss the implementation of shaping for DD-based methods. In Section VI, we conclude the paper.

II. PRELIMINARIES

A. Detection Methods

Table I lists the major detection methods used in optical communications following the classification scheme in [22]. The first three columns enumerate and describe five fundamentally different classes of detection methods, while the fourth and fifth columns specify, respectively, an LO-based implementation and a DD-based implementation for each class. Canonical receiver structures for most of these can be found in [22]. As defined here, an LO-based scheme injects an unmodulated carrier into the receiver to aid in detection, while a DD-based scheme does not (a DD-based scheme may transmit an unmodulated carrier along with the modulated signal to aid in detection). It should be evident from Table I that an LO-based scheme is not necessarily coherent; and, conversely, a DD-based scheme is not necessarily

TABLE I
MAJOR DETECTION METHODS IN OPTICAL COMMUNICATIONS

Classification	Detects	Signal Dimensions (in 2 Polarizations)	Local Oscillator- Based Method	Direct Detection- Based Method
Noncoherent	Intensity	1 or 2	Envelope detection	Standard direct detection
Differentially coherent	Differential phase shift	1 or 2	Delay-and-multiply detection	Delay interferometer detection
Noncoherent + differentially coherent hybrid	Stokes parameters	3	Polarization shift keying detection	3-D Stokes vector detection
Noncoherent + differentially coherent hybrid	Stokes parameters + differential phase shift	4	Polarization shift keying + delay-and- multiply detection	4-D Stokes vector detection
Coherent	Field quadratures	4	Standard coherent detection	Kramers Kronig detection

Shaping distributions for the methods in shaded boxes are studied in this paper.

noncoherent. For brevity, the discussion here is simplified from that in [22]; for example, frequency-shift keying and its variants are not discussed here.

It is instructive to discuss Table I row-by-row.

Noncoherent detection measures the intensity of signals (proportional to their energy or squared L_2 -norm of the electric field) in one or more orthogonal dimensions of a signal space, yielding one real decision statistic per dimension. Accordingly, single- or dual-polarization intensity-modulated signals respectively convey one or two real dimensions per symbol interval. Noncoherent detection can be achieved using LO-based downconversion followed by envelope detection [22], but is most commonly implemented using simple SD detection.

Differentially coherent detection measures phase differences between different orthogonal dimensions of a signal space, yielding one real decision statistic per pair of dimensions. It is typically used to detect differential phase-shift keying (DPSK), which encodes information in phase changes between successive symbols. Single- or dual-polarization DPSK signals respectively convey one or two real dimensions per symbol interval. Differentially coherent detection can be achieved using LO-based downconversion followed by delay-and-multiply detection [22], but is most commonly implemented using delay interferometers and DD.

The third row of Table I considers modulation of information in the SV [23], which can convey three real dimensions per symbol interval. Three-dimensional (3-D) SV modulation can be detected using LO-based polarization-shift keying detection or by DD-based SV detection [22], [23]. These detection methods are a hybrid between noncoherent and differentially coherent detection, since they measure intensities in, and phase differences between, two orthogonal polarizations [22]. As depicted in the fourth row, SV modulation can encode a fourth dimension per symbol by modulating the phase difference between successive symbols [39]. Methods for detecting 4-D SV modulation can also be considered hybrids between noncoherent and differentially coherent detection.

Coherent detection can measure the two electric field quadratures in each of the two polarizations, which can convey four real dimensions per symbol. It is typically implemented using LO-based downconversion with some means to synchronize the signal and LO carrier phases, which we refer to as SC detection. KK detection achieves coherent detection without requiring a LO [25], typically by transmitting a strong unmodulated carrier along with a modulated signal, detecting the received intensity and performing digital phase retrieval to obtain the received electric field. A dual-polarization system employing KK detection can convey nearly four real dimensions per symbol [27].

This tutorial paper studies the shaping distributions only for the four specific methods in shaded boxes in Table I. The only LO-based method studied is SC detection, which is studied in Section III. Three DD-based methods are studied: SD detection, 3-D SV detection and Kramers Kronig detection, which are studied in Section IV. Hereafter, 3-D SV detection is referred to simply as “SV detection”.

B. Assumptions and Performance Metrics

In this tutorial, we consider systems subject to average power constraints, which are relevant for a wide variety of system designs. In short-reach intra-data center fiber links [40] and in indoor free-space optical links [41], eye safety constrains average transmitted power. Likewise, in long-haul fiber links, fiber nonlinearity and optical amplifier pump power limitations can constrain average transmitted power [42].

Other works on shaping for DD systems consider other important constraints, such as peak power constraints or constraints on the average detected electrical power [24], [26], [43]. Indeed, these are important considerations for a wide range of systems. Our constraint on average optical power, however, is consistent with other fundamental studies of channel capacity, which start by considering average power constraints [14], [15], [16], [17], [18], [19], [33].

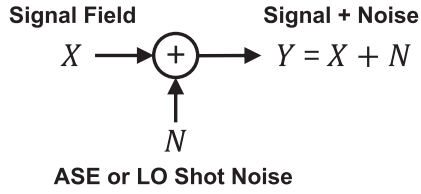


Fig. 1. Discrete-time channel model for single-polarization SC detection in the amplifier noise- or local oscillator shot noise-limited regime. The additive noise N is independent of X . ASE: Amplified spontaneous emission, LO: Local oscillator. Adapted from [45].

We study discrete-time channel models that consider one dominant additive noise in the thermal noise-limited or amplifier noise-limited regimes. A discrete-time channel model is explicitly presented for each receiver and noise regime combination studied. For simplicity, we do not consider cases where both thermal and amplifier noises are significant.

Our primary performance metric is achievable spectral efficiency given in terms of bits/symbol. We estimate the achievable spectral efficiency using mutual information, which implies no limits on encoding or decoding complexity, consistent with our focus on fundamental limits. We present results in terms of bits/symbol instead of bits/s/Hz, in part, due to the nonexistence of non-negative root-Nyquist pulses, which precludes the use of minimum-bandwidth pulses in SD systems [44]. This nonexistence may cause intersymbol interference, leading to dependence between successive uses of the discrete-time channel. We ignore these memory effects for analytical tractability and assume that each use of the discrete-time channel model is independent. While SV, KK and SC detection can detect bipolar signals, enabling use of root-Nyquist pulses that approach one bit/s/Hz, we use bits/symbol for all systems for the sake of consistency.

III. STANDARD COHERENT DETECTION

SC detection denotes LO-based coherent detection with additive white Gaussian noise (AWGN). In systems using optical amplifiers, this typically arises from LO-amplified spontaneous emission (ASE) beat noise, while in un-amplified systems, it arises from LO shot noise [22]. Assuming a single polarization for simplicity, SC detection is described by the discrete-time channel model in Fig. 1, and by the analytical model

$$Y = X + N. \quad (1)$$

Here, Y is the received complex electric field, X in the transmitted complex electric field, and N is an independent, zero-mean, additive complex circularly symmetric Gaussian random variable with variance $\text{var}(N) = 2\sigma_{\text{amp}}^2$. For concreteness, our notation assumes LO-ASE beat noise is dominant.

Shannon introduced an approach to computing the optimal input distribution for the SC channel which is based on maximizing mutual information, which we denote by the maximum mutual information (MMI) approach. In MMI, the channel capacity is defined as the maximum value of an objective function in a formally defined optimization problem [1]. In this framework,

the capacity-achieving input distribution is a solution to the formally stated optimization problem. While MMI is clearly defined and rigorous, the corresponding optimization problem can be solved analytically only for certain channel models. Despite the analytic intractability of the MMI problems for many channels, the optimal discrete input distribution can typically be computed numerically, as explained further in Section III-D.

Forney and Wei later extended HCA to channel coding to analytically compute continuous approximations to the optimal input distribution of the SC channel [31]. In the context of capacity-approaching high-dimensional coset codes, HCA determines an optimal shaping region to minimize the average power of enclosed signal points while maintaining a constant minimum distance. The input distribution for the channel input is obtained by marginalizing over the coset code. Forney and Wei's analysis was extended to study non-equiprobable signaling on the signal points contained by the optimal shaping region [46] and integration of shaping and coding [47].

In this section, we review both MMI and HCA and their application to the SC channel. In Section III-A, we briefly review MMI and introduce concepts and notation from information theory used throughout this paper. In Section III-B, we review the central concepts and methodologies in HCA. In Section III-C, we apply HCA to the SC channel, deriving the optimal input distribution and the shaping gain. Then, in Section IV, we extend HCA to study DD-based optical channels.

A. Maximum Mutual Information

The channel capacity was defined in [1] as the maximum mutual information between the input and output of a channel subject to various constraints on the channel input. In this tutorial, we consider discrete, memoryless channels with constraints on the average power of the channel input. The channel capacity for the average power-limited SC channel is

$$C = \max_{f_X(x): \mathbb{E}[|X|^2] \leq \bar{P}} I(X; Y), \quad (2)$$

where $f_X(x)$ is the probability density function (PDF) of X , \bar{P} is a constraint on the average power per symbol, \mathbb{E} is the expectation operator, and $I(X; Y) = h(Y) - h(Y|X)$ is the mutual information [48].

Using the independence of the signal and noise, the conditional entropy term can be simplified to $h(Y|X) = h(N)$. For the SC channel, maximizing the mutual information is equivalent to maximizing the entropy of the output distribution. Using variational calculus, one can show that the maximum-entropy distribution subject to a squared L_2 -norm constraint is the Gaussian distribution. Using the fact that the sum of two independent jointly Gaussian random variables is Gaussian distributed, the capacity-achieving input distribution is therefore a complex circularly symmetric Gaussian distribution, i.e.,

$$f_X(x) = \frac{1}{\pi \bar{P}} \exp\left(-\frac{1}{\bar{P}} \|x\|_2^2\right). \quad (3)$$

Using $X \sim \mathcal{CN}(0, \bar{P})$ in (2), the capacity of the SC channel is

$$C \left(\text{SNR}^{(\text{amp})} \right) = \log_2 \left(1 + \text{SNR}^{(\text{amp})} \right), \quad (4)$$

where $\text{SNR}^{(\text{amp})} = \bar{P}/2\sigma_{\text{amp}}^2$. Throughout this tutorial, the superscripts (th) and (amp) indicate that the dominant noises are additive thermal noise or additive amplifier noise, respectively.

B. High-Rate Continuous Approximation

As stated in Section I, attempting to apply MMI to study various DD channels in optical communications yields optimization problems that have not yet admitted analytical solution. HCA provides an approach for analytically approximating the optimal input distributions for these DD channels.

In this subsection, we review the central concepts and methodologies of HCA. While we aim to keep our presentation independent of the channel model, we assume the SC channel to ensure concreteness in our presentation. While referencing the SC channel throughout this subsection, we defer computation of the final analytical results for the SC channel until Section III-C.

Consider the discrete-time channel model for the SC channel in Fig. 1. For two arbitrary 1-D complex electric fields X_1 and X_2 input to the channel, the pairwise error probability under maximum-likelihood (ML) detection is

$$P_e(X_1, X_2) = Q\left(\frac{\|X_1 - X_2\|_2}{2\sigma_{\text{amp}}}\right). \quad (5)$$

In HCA, a signal point \mathbf{X} is an N -dimensional (N -D) complex vector formed by concatenating N time-disjoint symbols X_i , $i = 1, \dots, N$, i.e., $\mathbf{X} = [X_1, X_2, \dots, X_N]^T$. The pairwise error probability under ML detection for two arbitrary signal points \mathbf{X}_1 and \mathbf{X}_2 is

$$P_e(\mathbf{X}_1, \mathbf{X}_2) = Q\left(\frac{\|\mathbf{X}_1 - \mathbf{X}_2\|_2}{2\sigma_{\text{amp}}}\right). \quad (6)$$

The forms of (5) and (6) are the same because the additive noise is an independent, identically distributed Gaussian random variable in each vector component.

1) *Coset Code, Constellation, and Constituent Constellation:* The first step in HCA is to define a coset (translate of a lattice) from which a constellation can be constructed. For the sake of simplicity and notational convenience, we assume the coset is formed by the N -fold Cartesian product of a constituent coset. However, the analysis here applies to more general cosets.

Let $\Lambda^{(1)}$ and $\mathcal{C}\Lambda^{(1)}$ denote a real constituent coset and complex constituent coset, respectively. The number of dimensions in a constituent coset is determined by the number of independent dimensions in the detected signal of the discrete-time channel model. The constituent coset for the SC channel has one complex dimension, as one complex symbol is detected in any time interval. The other discrete-time channel models analyzed in this tutorial use different constituent cosets.

Let $\Lambda^{(N)}$ and $\mathcal{C}\Lambda^{(N)}$ denote real and complex cosets formed by the N -fold Cartesian product of $\Lambda^{(1)}$ and $\mathcal{C}\Lambda^{(1)}$, respectively. The dimensionalities of $\Lambda^{(N)}$ and $\mathcal{C}\Lambda^{(N)}$ are factors of N larger than the constituent cosets from which they are constructed.

A coset must be defined in terms of an underlying coordinate system. Following from (6), the coordinate system for the SC channel is the complex electric field because the pairwise error probability under ML detection is a decreasing function of

Euclidean distance in this coordinate system for any N . The SC channel uses the complex coset $\mathcal{C}\Lambda^{(N)}$.

A high-dimensional constellation is obtained from a coset by selecting all signal points in the coset that lie within a shaping region \mathcal{R} . In this tutorial, we restrict ourselves to closed, convex shaping regions. Let C denote the constellation formed by selecting all signal points from a coset that lie within \mathcal{R} . This operation is equivalent to the intersection operation between a coset and \mathcal{R} . For the SC channel, we have $C = \mathcal{C}\Lambda^{(N)} \cap \mathcal{R}$. In Section III-B2, we discuss the construction of optimized shaping regions.

The constituent constellation is defined as the set of points from the constituent coset that are used in at least one signal point from C . The constituent constellation is used extensively when discussing the induced density, which is introduced in Section III-B3.

Different channel models give rise to different coordinate systems, shaping regions, and constituent constellations. For example, as we will see in Section IV-B, shaping regions for the thermal noise-limited SD detection channel are defined in terms of a real N -D vector space with field intensity coordinates. The constituent constellation is a set of nonnegative intensity levels on \mathbb{R}_+^1 .

2) *Optimal Shaping Region and Continuous Approximation:* In HCA, the optimal shaping region is defined as the set of points whose physical energy is less than or equal to P . This region is optimal in that it encloses a given volume while minimizing average power. The mapping between the coordinates of a signal point and its physical energy depends on the coordinate system. Since the SC channel uses complex electric field coordinates, the physical energy of a signal point is its squared L_2 -norm. The optimal N -D shaping region for the SC channel with total physical energy at most P is

$$\mathcal{R}_{\text{shaped}}^{(\text{SC})}(N, P) = \{\mathbf{X} \in \mathbb{C}^N \mid \|\mathbf{X}\|_2^2 \leq P\}. \quad (7)$$

The reference shaping region is defined as an N -D hypercube in the same coordinate system at the optimal shaping region. The reference shaping region for the SC channel is parameterized by the maximum absolute value of any one side A and is therefore

$$\mathcal{R}_{\text{ref}}^{(\text{SC})}(N, A) = \left\{ \mathbf{X} \in \mathbb{C}^N \mid \left\| \left[\text{Re}\{\mathbf{X}\}, \text{Im}\{\mathbf{X}\} \right]^T \right\|_{\infty} \leq A \right\}, \quad (8)$$

where $\text{Re}\{\mathbf{X}\}$ and $\text{Im}\{\mathbf{X}\}$ are real N -D vectors formed by taking the real and imaginary parts of \mathbf{X} , respectively.

Fig. 2 shows an example constellation formed by the intersection of a coset and an optimal shaping region. For this example, we assume $\mathcal{C}\Lambda^{(N)}$ is the half-integer complex coset scaled to have minimum distance d . The optimal shaping region for $N = 1$ corresponds to a disk in the complex plane with radius \sqrt{P} . The set of points in the coset code is given by $C_{\text{shaped}}^{(\text{SC})}(N, P) = \mathcal{R}_{\text{shaped}}^{(\text{SC})}(N, P) \cap \mathcal{C}\Lambda^{(N)}$. The resulting constellation is optimal in the sense that it minimizes the average power subject of the constellation subject to a constraint on the number of points from the underlying coset that are included.

HCA simplifies the analysis of $\mathcal{R}_{\text{shaped}}^{(\text{SC})}(N, P)$ and $\mathcal{R}_{\text{ref}}^{(\text{SC})}(N, A)$ by using the continuous approximation. For

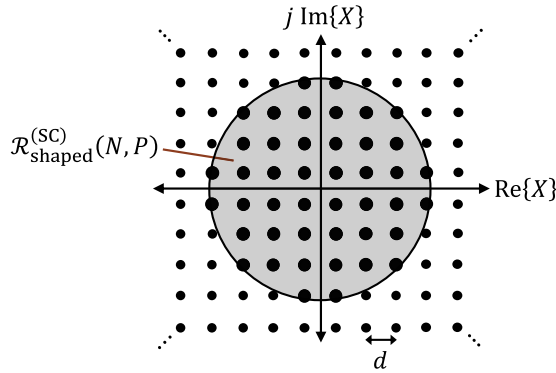


Fig. 2. Optimal constellation construction for the SC channel for $N = 1$ complex dimension. $\mathcal{C}\Lambda^{(N)}$ is the half-integer complex coset scaled to have minimum distance d and is depicted by the blue dots. $\mathcal{R}_{\text{shaped}}^{(\text{SC})}(N, P)$ is the continuous enclosed region and is depicted by the shaded region inside the circle. The constellation is the set of signal points from the coset that lie within the shaded region and is visually depicted by the 44 larger circles. Adapted from [45].

sufficiently dense constellations, the distribution of signal points in the constellation can be well-approximated by a continuous distribution over the shaping region [31], [33], [46], [47]. The continuous approximation replaces the uniform, discrete probability mass function over the signal points in the coset code with a uniform, continuous PDF over the shaping region that constructed the coset code.

Let $d\mathbf{x} = dx_{1I}, dx_{1Q}, dx_{2I}, dx_{2Q}, \dots, dx_{NI}, dx_{NQ}$, where x_{iI} and x_{iQ} are the real and imaginary parts of x_i , $i = 1, \dots, N$. Under HCA, the PDF for the shaping region is

$$f_{\mathbf{X}}(\mathbf{x}) = \frac{1}{\mathcal{V}_{\text{shaped}}^{(\text{SC})}(N, P)}, \quad \mathbf{x} \in \mathcal{R}_{\text{shaped}}^{(\text{SC})}(N, P), \quad (9)$$

where

$$\mathcal{V}_{\text{shaped}}^{(\text{SC})}(N, P) = \int_{\mathbf{x} \in \mathcal{R}_{\text{shaped}}^{(\text{SC})}(N, P)} d\mathbf{x}. \quad (10)$$

Similarly, the PDF for the reference region is

$$f_{\mathbf{X}}(\mathbf{x}) = \frac{1}{\mathcal{V}_{\text{ref}}^{(\text{SC})}(N, A)}, \quad \mathbf{x} \in \mathcal{R}_{\text{ref}}^{(\text{SC})}(N, A), \quad (11)$$

where

$$\mathcal{V}_{\text{ref}}^{(\text{SC})}(N, A) = \int_{\mathbf{x} \in \mathcal{R}_{\text{ref}}^{(\text{SC})}(N, A)} d\mathbf{x}. \quad (12)$$

The average powers of the shaped and reference constellations are given by the average squared L_2 -norm of the signal points in the two respective constellations. Under HCA, the average power of a constellation is approximated by the squared second moment of the shaping region. Let $\bar{P}_{\text{shaped}}^{(\text{SC})}(N, P)$ and $\bar{P}_{\text{ref}}^{(\text{SC})}(N, A)$ be the average power of the shaped and reference constellations under the continuous approximation, respectively. The general expressions for $\bar{P}_{\text{shaped}}^{(\text{SC})}(N, P)$ and $\bar{P}_{\text{ref}}^{(\text{SC})}(N, A)$ for the SC channel are

$$\bar{P}_{\text{shaped}}^{(\text{SC})}(N, P) = \frac{1}{\mathcal{V}_{\text{shaped}}^{(\text{SC})}(N, P)} \int_{\mathbf{x} \in \mathcal{R}_{\text{shaped}}^{(\text{SC})}(N, P)} \|\mathbf{x}\|_2^2 d\mathbf{x} \quad (13)$$

and

$$\bar{P}_{\text{ref}}^{(\text{SC})}(N, A) = \frac{1}{\mathcal{V}_{\text{ref}}^{(\text{SC})}(N, A)} \int_{\mathbf{x} \in \mathcal{R}_{\text{ref}}^{(\text{SC})}(N, A)} \|\mathbf{x}\|_2^2 d\mathbf{x}. \quad (14)$$

3) *Induced Marginal Density*: The induced marginal density on a basic signaling dimension is an important analytic result that can be derived using HCA. The shaping region affects the induced marginal distribution by defining the support region of the induced marginal distribution. The induced marginal density on a basic dimension can be obtained by marginalizing the joint PDF $f_{\mathbf{X}}(\mathbf{x})$ over all other dimensions. For concreteness, we compute the induced marginal density of X_1 , the first component of \mathbf{X} :

$$f_{X_1}(x) = \int_{-\infty}^{\infty} \cdots \int_{-\infty}^{\infty} f_{X_{1I}, X_{1Q}, \dots, X_{NQ}}(x_I, x_Q, \dots, x_{NQ}) d_{x_{2I}}, \dots, d_{x_{NQ}}. \quad (15)$$

One method for solving (15) is to partition \mathcal{R} into disjoint subsets and assign probability density proportional to the volumes of the subsets in the partition [32], [34], [35].

4) *Shaping Gain*: Shaping gain is a second important analytic result provided by HCA. The shaping gain is the factor of reduction in the average power of the optimal shaping region to the reference shaping region. The shaping gain $\gamma_s^{(\text{SC})}(N)$ is defined as

$$\gamma_s^{(\text{SC})}(N) \triangleq \frac{\bar{P}_{\text{ref}}^{(\text{SC})}(A)}{\bar{P}_{\text{shaped}}^{(\text{SC})}(N, P)}, \quad (16)$$

where P and A are chosen to ensure that $\mathcal{V}_{\text{shaped}}^{(\text{SC})}(N, P) = \mathcal{V}_{\text{ref}}^{(\text{SC})}(N, A)$. The variable N is dropped from $\bar{P}_{\text{ref}}^{(\text{SC})}(N, A)$ to obtain $\bar{P}_{\text{ref}}^{(\text{SC})}(A)$ because $\bar{P}_{\text{ref}}^{(\text{SC})}(N, A)$ does not depend on N . The ultimate shaping gain $\gamma_s^{(\text{SC})}$ is defined as the shaping gain in the limit as $N \rightarrow \infty$:

$$\gamma_s^{(\text{SC})} \triangleq \lim_{N \rightarrow \infty} \gamma_s^{(\text{SC})}(N). \quad (17)$$

The average power of the reference shaping region is an expectation of a function of the marginal density, which is the uniform distribution. The specific function is the physical energy of the signal point, which is the squared L_2 -norm in the case of SC detection.

The average power of the optimal shaping region can be computed by exploiting the properties of $\mathcal{R}_{\text{shaped}}^{(\text{SC})}(N, P)$. The fraction of signal points in $\mathcal{R}_{\text{shaped}}^{(\text{SC})}(N, P)$ with power at most p is $\mathcal{V}_{\text{shaped}}^{(\text{SC})}(N, p) / \mathcal{V}_{\text{shaped}}^{(\text{SC})}(N, P)$. Let random variable ρ be the total optical power of a signal point selected uniformly from $\mathcal{R}_{\text{shaped}}^{(\text{SC})}(N, P)$. The CDF of ρ for SC detection is

$$F_{\rho}(p) = \frac{\mathcal{V}_{\text{shaped}}^{(\text{SC})}(N, p)}{\mathcal{V}_{\text{shaped}}^{(\text{SC})}(N, P)}, \quad p \in [0, P]. \quad (18)$$

The average optical power can be computed as the normalized expectation of ρ . Computing the average optical power of the optimal constellation using the distribution of ρ is a general strategy that also applies to optimal shaping regions for other detection methods.

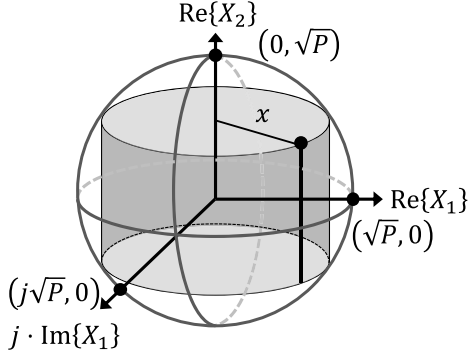


Fig. 3. Optimal SC detection shaping region for $N = 1.5$ complex dimensions. The vertical black line corresponds to the set of signal points enclosed by the shaping region that satisfies the constraint $X_1 = x$. Adapted from [45].

C. High-Rate Continuous Approximation for Standard Coherent Detection

The channel model for SC detection was given in Fig. 1 and (1). In view of (6), the complex electric field is chosen as our coordinate system.

1) *Shaping Regions*: The next step in HCA is to define optimal and reference shaping regions. From these shaping regions, we can compute closed-form expressions for $\mathcal{V}_{\text{shaped}}^{(\text{SC})}(N, P)$, $\mathcal{V}_{\text{ref}}^{(\text{SC})}(N, A)$, $\bar{P}_{\text{shaped}}^{(\text{SC})}(N, P)$, and $\bar{P}_{\text{ref}}^{(\text{SC})}(A)$.

The optimal and reference shaping regions for the SC channel are given in (7) and (8), respectively. Fig. 3 shows the optimal shaping region in $N = 1.5$ complex dimensions, which is a real 3-D ball with radius \sqrt{P} . In N complex dimensions, the optimal shaping region is a $2N$ -real-dimensional ball with radius \sqrt{P} .

The volume of $\mathcal{R}_{\text{shaped}}^{(\text{SC})}(N, P)$ is equal to the volume of a $2N$ -D real ball with radius \sqrt{P} and is

$$\mathcal{V}_{\text{shaped}}^{(\text{SC})}(N, P) = \frac{(\pi P)^N}{N!}. \quad (19)$$

The volume of $\mathcal{R}_{\text{ref}}^{(\text{SC})}(N, A)$ is the volume of a $2N$ -D real hypercube with side length $2A$ and is

$$\mathcal{V}_{\text{ref}}^{(\text{SC})}(N, A) = (2A)^{2N}. \quad (20)$$

Using (19) in (18), we obtain

$$F_{\rho}(p) = \left(\frac{p}{P}\right)^N, \quad \rho \in [0, P]. \quad (21)$$

The average power of the optimal shaping region is

$$\bar{P}_{\text{shaped}}^{(\text{SC})}(N, P) = \frac{1}{N} \mathbb{E}[\rho] = \frac{P}{N+1}. \quad (22)$$

The average power of the reference shaping region is

$$\bar{P}_{\text{ref}}^{(\text{SC})}(A) = \frac{2}{3} A^2. \quad (23)$$

2) *Induced Distribution*: The general analytical form for the marginal density is given in (15). The remaining step is to evaluate the marginal distribution for the SC channel. Detailed derivations can be found in [31], [45].

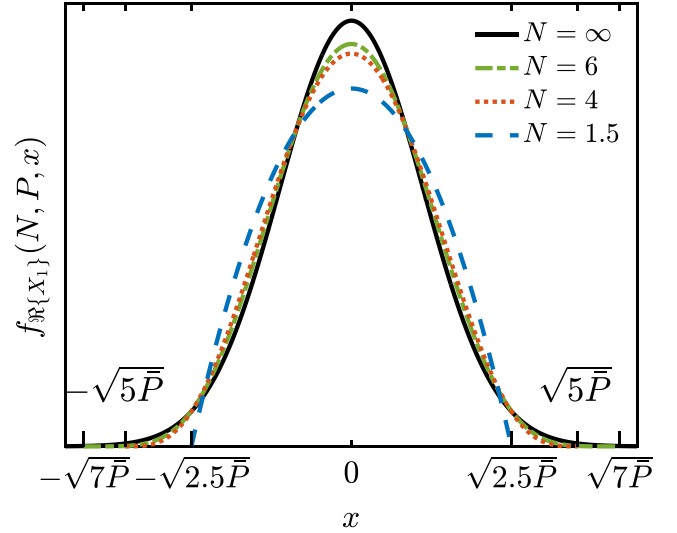


Fig. 4. Marginal density induced on $\text{Re}\{X_1\}$ by the optimal shaping region for SC detection for various N . For finite and infinite N , expressions for the marginal density are given in (24) and (25), respectively. $f_{\text{Re}\{X_1\}}(N, P, x)$ converges to a Gaussian distribution as $N \rightarrow \infty$. $\bar{P} = \mathbb{E}[|X_1|^2]$ is fixed to a constant value as N is varied.

One can show that the induced distribution must satisfy the following proportionality:

$$f_{X_1, \text{shaped}}^{(\text{SC})}(N, P, x) \propto \left(1 - \frac{|x|^2}{(N+1)\bar{P}_{\text{shaped}}^{(\text{SC})}(N, P)}\right)^{N-1}, \quad |x|^2 \in [0, P]. \quad (24)$$

Using $\bar{P}_{\text{shaped}}^{(\text{SC})}(N, P) = \mathbb{E}[|X_1|^2]$ and taking the limit as $N \rightarrow \infty$, we find

$$f_{X_1, \text{shaped}}^{(\text{SC})}(x) \triangleq \lim_{N \rightarrow \infty} f_{X_1, \text{shaped}}^{(\text{SC})}(N, P, x) \propto \exp\left(\frac{-|x|^2}{\mathbb{E}[|X_1|^2]}\right), \quad x \in \mathbb{C}. \quad (25)$$

We conclude that the optimal shaping region for SC detection induces a circularly symmetric complex Gaussian density as $N \rightarrow \infty$.

We can also analyze the induced density on X_1 for intermediate values of N . First, we write X_1 in terms of its real and imaginary parts as $X_1 = \text{Re}\{X_1\} + j\text{Im}\{X_1\}$. Fig. 4 shows the induced marginal density of $\text{Re}\{X_1\}$ for different values of N . The induced marginal density on $\text{Re}\{X_1\}$ for a given N is

$$f_{\text{Re}\{X_1\}}(N, P, x) = \int_{-\infty}^{\infty} f_{X_1, \text{shaped}}^{(\text{SC})}(N, P, x + jy) dy. \quad (26)$$

We also define $f_{\text{Im}\{X_1\}}(N, P, x)$ by similarly marginalizing over $\text{Re}\{X_1\}$. By symmetry, $f_{\text{Re}\{X_1\}}(N, P, x) = f_{\text{Im}\{X_1\}}(N, P, x)$, so we only plot the marginal density for $\text{Re}\{X_1\}$ for sake of simplicity.

We include the case of $N = 1.5$ to show the density induced by the shaping region in Fig. 3. While the density induced in

X_1 traces out a hemisphere with radius $\sqrt{2.5\bar{P}}$ for $N = 1.5$, the density induced on $\text{Re}\{X_1\}$ is not a half-circle. The marginalization over $\text{Im}\{X_1\}$ causes the induced density on $\text{Re}\{X_1\}$ to no longer trace a half-circle. The intermediate values of $N = 4$ and $N = 6$ visually show the density converges toward a Gaussian distribution. It is important to note that the maximum value for $\text{Re}\{X_1\}$ must increase with $\sqrt{N+1}$ to maintain constant average power.

3) *Shaping Gain*: Now we compute a closed-form expression for the ultimate shaping gain for SC detection. The expression for the ultimate shaping gain was first given in (17). The computation of the ultimate shaping gain only requires the volume expressions (19) and (20) and the average power expressions (22) and (23).

We first need to equate the volumes of the optimal and reference shaping regions. Equating (20) and (19), using Stirling's approximation, taking the ratio of (23) to (22) and letting $N \rightarrow \infty$, we obtain

$$\gamma_s^{(\text{SC})} = \frac{\pi e}{6} \approx 1.53 \text{ dB}. \quad (27)$$

D. Numerical Optimization of the Input Distribution

MMI and HCA provide closed-form analytic expressions for the optimal input distribution and channel capacity for SC detection. These techniques, however, presume signaling techniques and operating regimes that may not always apply in practice. For example, MMI and HCA presume continuous constellations, in contrast with the discrete constellations used in practice. HCA also presumes operation in the high-SNR regime, which is not always applicable.

Numerical estimation of the channel capacity provides an analysis that is complementary to the analytical results derived using MMI and HCA. For example, numerical methods can estimate the achievable information rates when finite, discrete constellations are used or under various input probability distribution constraints. Numerical methods can also independently verify the ultimate shaping gains and induced marginal densities derived using MMI and HCA.

In this subsection, we first define the coded modulation capacity of the SC channel. We then present a general procedure for computing optimized discrete input distributions that can be used for both the SC channel and DD channels. We then numerically analyze the coded modulation capacity of the SC channel for various M and different constraints on the input distributions. In Section IV, we use similar procedures to study the coded modulation capacity for several DD-based methods.

1) *Coded Modulation Capacity*: The coded modulation capacity is a definition of channel capacity applicable when the constellation input to the channel is discrete [49]. Let $C_{\text{ref}}^{(\text{SC})}(M)$ be a minimum-energy cubic constellation with M signal points selected from $C_{\text{ref}}^{(\text{SC})}(N, A)$. M is restricted to positive integers that allow the constellation to have symmetry about the mirror

planes passing through the coordinate axes. The coded modulation capacity for the SC channel is

$$C_{\text{CM}}^{(\text{SC})}(\text{SNR}^{(\text{amp})}, M) \triangleq \max_{\substack{\sigma_{\text{amp}}, P_X(x): \\ \frac{\mathbb{E}\{|X|^2\}}{\sigma_{\text{amp}}^2} \leq \text{SNR}^{(\text{amp})} \\ \mathcal{X} = C_{\text{ref}}^{(\text{SC})}(M)}} I(X; Y), \quad (28)$$

where M is the modulation order, $P_X(x)$ is a probability mass function (PMF) over the input constellation, and \mathcal{X} is the alphabet of the random variable X .

In the optimization (28), the constellation has a fixed unit spacing. We optimize the input distribution $P_X(x)$ to maximize mutual information, while simultaneously optimizing the noise standard deviation σ_{amp} to achieve the SNR constraint $\text{SNR}^{(\text{amp})}$. In an equivalent formulation, one may fix σ_{amp} and achieve the SNR constraint by optimizing over the constellation spacing using a scale factor $\lambda > 0$ [49]. In this paper, we fix $\lambda = 1$ and optimize over σ_{amp} .

2) *Numerical Optimization of the Input Distribution*: Numerically solving (28) requires a method of computing the optimal $P_X(x)$. The Blahut-Arimoto (BA) algorithm can be used to compute the capacity-achieving input distribution for arbitrary discrete memoryless channels subject to an average power constraint [11], [12]. To use the BA algorithm in (28), the continuous-valued output of the channel must be quantized. Throughout this paper, we use the method described in [50] to compute the correct number of output bins. For any fixed value of σ_{amp} in (28), the optimal input distribution can be found using the BA algorithm. The complete optimization can be solved by adding an outer loop to optimize over $\sigma_{\text{amp}} > 0$.

While the BA algorithm can numerically compute the optimal input distribution, we are also interested in evaluating the coded modulation capacity under additional constraints on the input distribution. For example, it is often desirable to parameterize the input distribution by one or more variables. Such an approach reduces implementation complexity in practice and facilitates comparison with the optimal input distribution computed by the BA algorithm and other analytic distributions.

The following presents a general procedure for obtaining a parameterized discrete input distribution from a continuous Gaussian, exponential, or uniform distribution. While we use these discrete distributions here to analyze the SC channel, this procedure is also used to obtain discrete input distributions for several DD channels in Section IV. The continuous Gaussian distribution is assumed to be a zero-mean, N -D IID real or circularly symmetric complex Gaussian random vector and is proportional to

$$f_{\mathbf{X}}(\mathbf{x}, \beta) \propto \exp\left(-\beta \|\mathbf{x}\|_2^2\right), \quad (29)$$

where $\beta \geq 0$ is a shaping parameter. The continuous exponential distribution is a zero-mean real or complex random variable and assigns probability proportional to

$$f_{\mathbf{X}}(\mathbf{x}, \beta) \propto \exp(-\beta \|\mathbf{x}\|_2). \quad (30)$$

The continuous uniform distribution is not parameterized by β .

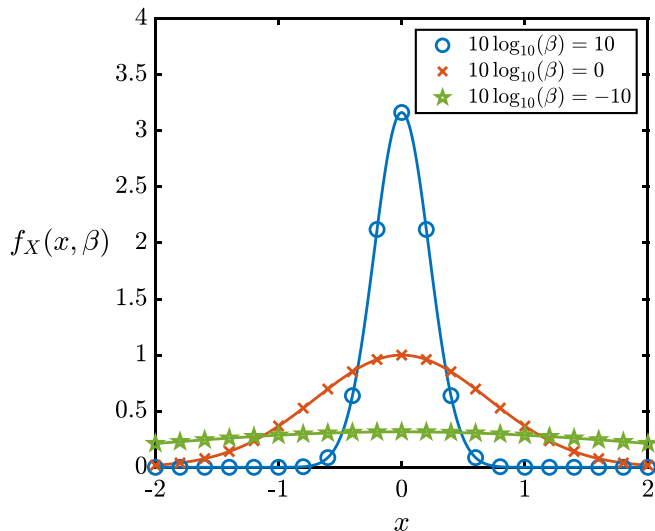


Fig. 5. Continuous 1-D Gaussian probability density function $f_X(x, \beta)$ vs. x for shaping parameter values $10 \cdot \log_{10}(\beta) = 10, 0,$ and -10 given in (29). The 21 markers on each curve indicate locations of samples of the continuous distribution, which are normalized according to (31) to obtain a Maxwell-Boltzmann distribution. Adapted from [45].

The continuous Gaussian, exponential, and uniform distributions must be sampled and normalized to obtain discrete PMFs. The associated discrete PMFs for the Maxwell-Boltzmann (MB) and exponential distributions $P_{\mathbf{X}}(\mathbf{x}, \beta)$ with alphabet \mathcal{X} are obtained by sampling and normalizing the continuous PDFs for each value in the alphabet, i.e.,

$$P_{\mathbf{X}}(\mathbf{x}, \beta) = \frac{f_{\mathbf{X}}(\mathbf{x}, \beta)}{\sum_{\mathbf{x}' \in \mathcal{X}} f_{\mathbf{X}}(\mathbf{x}', \beta)}. \quad (31)$$

The discrete uniform distribution assigns probability $1/|\mathcal{X}|$ to each $\mathbf{x} \in \mathcal{X}$.

Fig. 5 shows an example of sampling a 1-D continuous Gaussian distribution and normalizing for three different values of β to obtain an MB distribution [46]. For larger values of β , more probability is concentrated near $x = 0$. As β decreases, the normalized discrete distribution converges to a uniform distribution.

The coded modulation capacity expression (28) can be easily adapted to include constraints on the input distribution. In the case of the discrete uniform distribution, there is only one valid PMF, which in turn fixes the value of σ_{amp} . The uniform input distribution constraint therefore reduces the optimization in (28) to a simple Monte Carlo estimate of the empirical mutual information.

In the case of either the MB distribution or discrete exponential distribution, (28) becomes an optimization over $\sigma_{\text{amp}} > 0$ and $\beta \geq 0$. However, for each β , there exists only one value of σ_{amp} that satisfies the SNR constraint. Thus, the optimization in (28) becomes a simple 1-D parameter search over $\beta \geq 0$.

In this paper, a subset of the optimal, MB, exponential, and uniform distributions are numerically computed for each of the channels analyzed. The term *optimal* indicates that the BA algorithm is used to obtain the input distribution. The terms

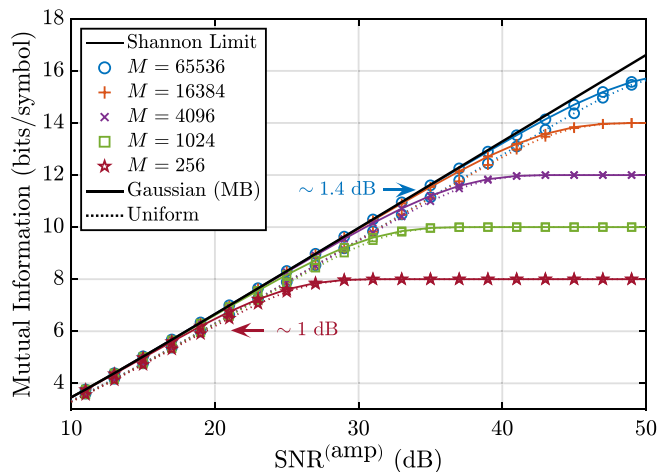


Fig. 6. Mutual information vs. $\text{SNR}^{(\text{amp})}$ for SC detection for varying modulation order M and uniform square constellations. The solid and dotted lines indicate that the transmitted signal points follow a Gaussian (Maxwell-Boltzmann (MB)) or uniform distribution, respectively. The blue and red arrows and text indicate the values of $\text{SNR}^{(\text{amp})}$ and mutual information at which the maximum shaping gains are obtained for modulation orders for $M = 65536$ and $M = 256$, respectively.

Maxwell-Boltzmann and *exponential* indicate that an optimization of the shaping parameter β , the noise variance, and sampling as described in (31) is used to obtain the input distribution. The term *uniform* indicates the mutual information is obtained via Monte Carlo simulation with a fixed discrete uniform input distribution.

3) *Numerical Analysis for Standard Coherent Detection:* The HCA analysis for the induced marginal density and ultimate shaping gain implies that the continuous 2-D complex Gaussian distribution is 1.53 dB more energy efficient than the continuous 2-D uniform distribution at the same information rate. In practice, discrete 2-D constellations per polarization are used. In this section, we analyze the achievable shaping gains using finite square constellations with modulation order M .

Fig. 6 shows MI vs. $\text{SNR}^{(\text{amp})}$ for the SC channel. Modulation orders $M = 65536$, $M = 16384$, $M = 4096$, $M = 1024$, and $M = 256$ are differentiated by unique markers. The solid and dotted lines indicate whether the MB or uniform distributions are used, respectively. The MI achieved using the BA algorithm is indistinguishable from the MB input distribution, so only the MB distribution is shown. The Shannon limit is included as a reference and is given by $\log_2(1 + \text{SNR}^{(\text{amp})})$ bits/symbol.

The finite-constellation shaping gains for $M = 65536$ and $M = 256$ are indicated by the blue and red arrows and text in Fig. 6. This finite-constellation shaping gain is computed by computing the largest difference in $\text{SNR}^{(\text{amp})}$ between the uniform distribution and the MB distribution at a fixed MI over the range of $\text{SNR}^{(\text{amp})}$ analyzed. The finite-constellation shaping gain increases from ~ 1 dB to ~ 1.4 dB as M increases from 256 to 65536. The relative increase in shaping gain decreases for each factor of 4 increase in M . The finite-constellation shaping gain for $M = 65536$ is ~ 0.13 dB less than the ultimate shaping gain given in (27). This gap could be decreased by further increasing M .

IV. DIRECT-DETECTION METHODS

In this section, we explain how to derive continuous-valued induced marginal densities for several important DD-based methods. As a first step, in Section IV-A, we introduce the concept of natural coordinates. We then use HCA to derive input distributions for thermal noise-limited and amplifier noise-limited SD detection and SV detection in Section IV-B through Section IV-E. Finally, in Section IV-F, we use MMI to study the optimal input distribution for amplifier noise-limited KK detection.

A. Natural Coordinates

Natural coordinates are a key to applying HCA to DD-based methods, particularly in the amplifier noise-limited regime, where the detected noise is signal-dependent. The term *natural coordinates* [34] refers to a coordinate system in which a set of signals may be expressed such that the pairwise error probability between any two signals is a decreasing function of the Euclidean distance between them, at least asymptotically at high SNR. When a coset is expressed in natural coordinates, the minimum Euclidean distance characterizes the pairwise error probability between nearest neighbors throughout the coset, and remains a good descriptor of the nearest-neighbor error probability when the coset is approximated by a continuum with uniform density.

Although Forney and Wei did not explicitly define the natural coordinates, they may be considered implicit in their treatment of shaping for SC detection [31], where the natural coordinates are the electric field quadratures, and the physical energy of a signal corresponds to its squared L_2 -norm.

For the various DD-based methods studied here, the natural coordinates depend on the detection method, the noise distribution, and the decision rule, and are not necessarily the same as the physical variables that are modulated or detected. Depending on the natural coordinates in which a signal is expressed, its physical energy does not necessarily correspond to its squared L_2 -norm.

For example, in thermal noise-limited SD detection [32], we modulate electric field magnitude or intensity and detect intensity. The natural coordinates for describing a signal (coset point) are the sequence of intensities, and the physical energy of a signal is its L_1 -norm. By contrast, in amplifier noise-limited SD detection [34], we modulate electric field magnitude or intensity and detect intensity. The natural coordinates are the sequence of electric field magnitudes, and the physical energy of a signal is its squared L_2 -norm.

In general, the statistics of the dominant noise source affect the induced marginal density and shaping gain by affecting the natural coordinates of the discrete-time channel. The pairwise error probability being a Q-function of the Euclidean distance is a sufficient condition to establish the natural coordinates and approximately holds for every discrete-time channel model studied in this paper. We also note that the natural coordinates derived for each discrete-time channel model are not unique, as the L_2 -norm is preserved under any unitary transformation of the natural coordinates.

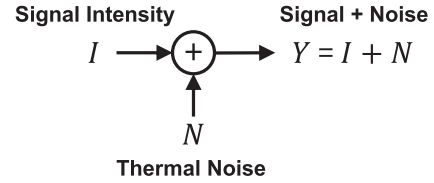


Fig. 7. Discrete-time channel model for SD detection in the thermal noise-limited regime. The noise variance σ_{th}^2 is independent of I . Adapted from [45].

In the various DD-based methods studied in the following subsections, the natural coordinates are derived using a variety of observations and approximations, so we defer more detailed explanation of the natural coordinates to those subsections.

B. Standard Direct Detection, Thermal Noise-Limited

The first work on probabilistic shaping for optical communications used HCA to analytically approximate the optimal input distribution for SD detection of intensity-modulated signals in the thermal noise-limited regime [32]. This calculation is reviewed in this subsection.

The discrete-time channel model for SD detection in the thermal noise-limited regime is shown in Fig. 7 and is given by

$$Y = I + N. \quad (32)$$

The detected electrical signal Y is equal to the signal intensity $I \geq 0$ corrupted by signal-independent Gaussian noise N with variance σ_{th}^2 .

1) *Natural Coordinates*: Given two possible signal intensities in a symbol interval, I_1 and I_2 , the pairwise error probability under ML detection is

$$P_e(I_1, I_2) = Q\left(\frac{\|I_1 - I_2\|_2}{2\sigma_{\text{th}}}\right). \quad (33)$$

The error probability (33) is a decreasing function of the Euclidean distance between I_1 and I_2 , implying that the natural coordinates for thermal noise-limited SD detection are intensities.

2) *Shaping Regions*: Let $\mathbf{I} = [I_1, I_2, \dots, I_N]^T \in \mathbb{R}_+^N$ be a real N -D vector be formed by concatenating N 1-D signal intensities in N disjoint symbol intervals. The average optical power of \mathbf{I} is $\frac{1}{N}\|\mathbf{I}\|_1$. The optimal shaping region consists of the set of N -D signal points with peak total power at most P :

$$\mathcal{R}_{\text{shaped}}^{(\text{SD,th})}(N, P) = \{\mathbf{I} \in \mathbb{R}_+^N \mid \|\mathbf{I}\|_1 \leq P\}. \quad (34)$$

This region is depicted for the case of $N = 3$ in Fig. 8, and is a tetrahedron. More generally, the shaping region is an N -simplex in N dimensions. The volume of $\mathcal{R}_{\text{shaped}}^{(\text{SD,th})}(N, P)$ is

$$\mathcal{V}_{\text{shaped}}^{(\text{SD,th})}(N, P) = \frac{P^N}{N!}. \quad (35)$$

The average optical power of $\mathcal{R}_{\text{shaped}}^{(\text{SD,th})}(N, P)$ is

$$\bar{P}_{\text{shaped}}^{(\text{SD,th})}(N, P) = \frac{P}{N+1}. \quad (36)$$

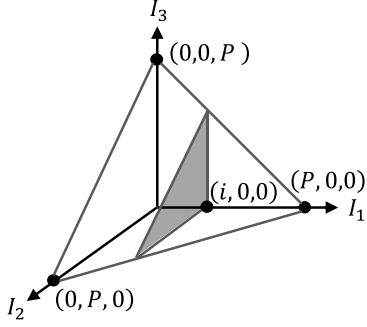


Fig. 8. Thermal noise-limited SD detection: Optimal shaping region in $N = 3$ real dimensions. The shaded region depicts the set of points from the shaping region that satisfy the constraint $I_1 = i$. Adapted from [45].

The reference shaping region is defined by a hypercube in the intensity. This shaping region can be equivalently described as the set of signal points with a peak intensity constraint A on each constituent 1-D symbol, and is given by

$$\mathcal{R}_{\text{ref}}^{(\text{SD,th})}(N, A) = \{\mathbf{I} \in \mathbb{R}_+^N \mid \|\mathbf{I}\|_{\infty} \leq A\}. \quad (37)$$

The volume of the region is simply

$$\mathcal{V}_{\text{ref}}^{(\text{SD,th})}(A) = A^N. \quad (38)$$

Because each signaling dimension is independent, the average optical power of the shaping region can be computed by the expectation of the intensity in any one dimension, and is

$$\bar{P}_{\text{ref}}^{(\text{SD,th})}(A) = \frac{A}{2}. \quad (39)$$

3) *Induced Distribution and Shaping Gain:* The induced density in one basic dimension must satisfy the following [32]:

$$f_{I_1}(N, P, i) \propto \left(1 - \frac{i}{(N+1)\bar{P}_{\text{shaped}}^{(\text{SD,th})}(N, P)}\right)^{N-1}, \quad i \in [0, P]. \quad (40)$$

Using $\bar{P}_{\text{shaped}}^{(\text{SD,th})}(N, P) = \mathbb{E}[I_1]$ and taking the limit as $N \rightarrow \infty$, we find

$$f_{I_1}(i) = \lim_{N \rightarrow \infty} f_{I_1}(N, P, i) \propto \exp\left(\frac{-i}{\mathbb{E}[I_1]}\right), \quad i \in \mathbb{R}_+. \quad (41)$$

The optimal shaping region for the thermal noise-limited SD receiver induces an exponential distribution in the intensity. This is equivalent to a Rayleigh distribution in the electric field magnitude.

We now compute the ultimate shaping gain for the thermal noise-limited SD receiver. Setting the volumes of the shaped and reference regions in (35) and (38) equal and using Stirling's approximation, we find the ultimate shaping gain to be

$$\gamma_s^{(\text{SD,th})} = \lim_{N \rightarrow \infty} \frac{\bar{P}_{\text{ref}}^{(\text{SD,th})}(A)}{\bar{P}_{\text{shaped}}^{(\text{SD,th})}(N, P)} = \frac{e}{2}. \quad (42)$$

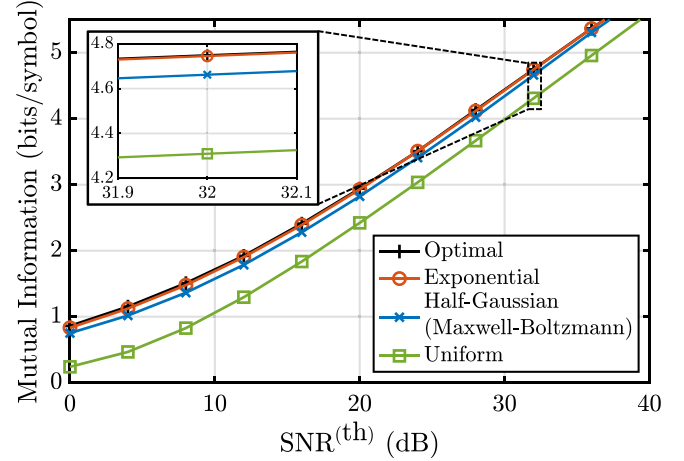


Fig. 9. Mutual information vs. $\text{SNR}^{(\text{th})}$ for the thermal noise-limited SD detection channel. The 128-point constellations are uniformly spaced in intensity. Adapted from [45].

Fig. 9 shows mutual information vs. $\text{SNR}^{(\text{th})} = \bar{P}^2 / \sigma_{\text{th}}^2$ for thermal noise-limited SD detection using 128-point constellations uniformly spaced in intensity with optimal, exponential, MB and uniform input distributions. The optimal distribution and its mutual information are computed numerically using the BA method, as explained in Section III-D. Consistent with the HCA analysis, an exponential distribution in intensity outperforms a MB distribution in intensity at all values of $\text{SNR}^{(\text{th})}$ shown. The exponential distribution achieves a mutual information within 0.03 bits/symbol of the optimal distribution over the entire range of SNRs studied, with the gap decreasing as $\text{SNR}^{(\text{th})}$ increases. The empirical shaping gain at 5 bits/symbol is 2.65dB, which is close to the ultimate shaping gain of $2 \times 10 \log_{10}(e/2) \approx 2.665$ dB in (42) when expressed in terms of $\text{SNR}^{(\text{th})}$.

Over the range of $\text{SNR}^{(\text{th})}$ studied in Fig. 9, the shaping gain for the optimal input distribution decreases monotonically with increasing $\text{SNR}^{(\text{th})}$. This is in contrast with SC detection, where the shaping gain increases monotonically toward its maximum value as $\text{SNR}^{(\text{amp})}$ increases. This is a consequence of the discreteness of the optimal input distribution for thermal noise-limited SD detection [14], [16]. At low values of $\text{SNR}^{(\text{th})}$, optimization over the thermal noise standard deviation σ_{th} leads to a large separation between adjacent constellation points relative to σ_{th} , with the result that only a few constellation points have significant probability, despite the simulation including many possible constellation points.

C. Standard Direct Detection, Amplifier Noise-Limited

In this subsection, we review the application of HCA to amplifier noise-limited SD detection [34]. The discrete-time channel model is shown in Fig. 10, and is given by

$$\begin{aligned} Y &= |X + N|^2 \\ &= |X|^2 + 2\text{Re}(X^*N) + |N|^2. \end{aligned} \quad (43)$$

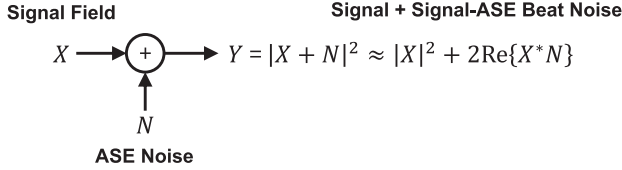


Fig. 10. Discrete-time channel model for SD detection in the amplifier noise-limited regime. The approximation, made at high SNR, neglects ASE-ASE beat noise. The signal-ASE beat noise variance $\sigma_{2\text{Re}\{X^*N\}}^2$ is proportional to the signal energy $|X|^2$. ASE: Amplified spontaneous emission. Adapted from [45].

For simplicity, we have assumed the signal and ASE are received in one polarization. This enables us to write the channel model in (43) as a complex, scalar channel. The signal X is generally complex-valued, and the ASE noise N is a complex circularly symmetric ASE noise with variance $2\sigma_{\text{amp}}^2$, i.e., $N \sim \mathcal{CN}(0, 2\sigma_{\text{amp}}^2)$. The signal component of the detected intensity Y is proportional to $|X|^2$. Because the phase of X is lost in detection, we may assume X is real and nonnegative, and use X and $|X|$ interchangeably, without changing the statistics of the detected intensity Y .

The detected intensity Y includes additive noise components $\text{Re}(X^*N)$ and $|N|^2$, which are, respectively, signal-ASE and ASE-ASE beat noises. In the high-SNR regime, the signal-ASE beat noise is dominant, and the ASE-ASE beat noise becomes negligible. The discrete-time channel model is approximated by

$$\begin{aligned} Y &\approx |X|^2 + 2\text{Re}(X^*N) \\ &= |X|^2 + \tilde{N}, \end{aligned} \quad (44)$$

where the signal-ASE beat noise is $\tilde{N} = 2\text{Re}(X^*N)$. In the HCA derivation, we use the approximate channel model (44). Our numerical simulations to evaluate mutual information use the exact channel model (43), which includes both signal-ASE and ASE-ASE beat noises.

1) *Natural Coordinates*: Consider two arbitrary electric fields x_1 and x_2 input to the channel modeled by (44). The signal-ASE beat noise is Gaussian distributed with a variance that scales linearly with received optical intensity. The conditional distributions of this noise are $\tilde{N}|(X = x_i) \sim \mathcal{N}(0, \sigma_i^2)$, where $\sigma_i^2 = 4|x_i|^2\sigma_{\text{amp}}^2$ for $i = 1, 2$.

The conditional distributions of the detected intensity are $Y|(X = x_i) \sim \mathcal{N}(x_i, \sigma_i^2)$ for $i = 1, 2$. The exact ML decision threshold is a value of Y at which the two conditional distributions of Y cross. The ML decision threshold is well approximated by the simple formula

$$Y_d = \frac{\sigma_1|x_2|^2 + \sigma_2|x_1|^2}{\sigma_1 + \sigma_2} = |x_1||x_2|. \quad (45)$$

Let $P_e(x_1|x_2)$ be the probability of decoding x_1 given x_2 was transmitted and $P_e(x_2|x_1)$ is defined likewise. Using the decision threshold (45), we find $P_e(x_1|x_2) = P_e(x_2|x_1)$. Therefore, the pairwise error probability between x_1 and x_2 is

$$P_e(x_1, x_2) = P_e(x_1|x_2) = P_e(x_2|x_1) \quad (46)$$

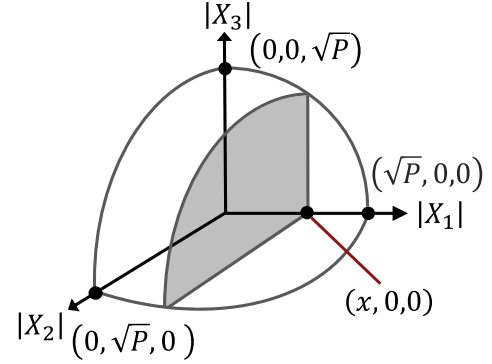


Fig. 11. Amplifier noise-limited SD detection: Optimal shaping region for $N = 3$ real dimensions. Adapted from [45].

$$= Q\left(\frac{\| |x_2| - |x_1| \|_2}{2\sigma_{\text{amp}}}\right). \quad (47)$$

Since the pairwise error probability is given by a Q-function of the L_2 -norm of the difference in electric field magnitudes, we conclude that electric field magnitudes are natural coordinates for the amplifier noise-limited SD receiver.

2) *Shaping Regions*: Let $\mathbf{X} = [X_1, X_2, \dots, X_N]^T \in \mathbb{R}_+^N$ be a real N -D vector be formed by concatenating N 1-D electric field magnitudes in N disjoint symbol intervals. The average optical power of \mathbf{X} is $\frac{1}{N}\|\mathbf{X}\|_2^2$. The optimal shaping region is the set of N -D signal points with peak total power P :

$$\mathcal{R}_{\text{shaped}}^{(\text{SD,amp})}(N, P) = \left\{ \mathbf{X} \in \mathbb{R}_+^N \mid \|\mathbf{X}\|_2^2 \leq P \right\}. \quad (48)$$

Fig. 11 shows the optimal shaping region for the amplifier noise-limited SD receiver for $N = 3$, which is the intersection of a 3-D ball with the non-negative orthant. For general N , the shaping region is the intersection between an N -D ball and the non-negative orthant. The volume of the region $\mathcal{R}_{\text{shaped}}^{(\text{SD,amp})}(N, P)$ is

$$\mathcal{V}_{\text{shaped}}^{(\text{SD,amp})}(N, P) = \frac{1}{\Gamma(\frac{N}{2} + 1)} \frac{(\pi P)^{N/2}}{2^N}. \quad (49)$$

The average optical power of the region $\mathcal{R}_{\text{shaped}}^{(\text{SD,amp})}(N, P)$ is

$$\bar{P}_{\text{shaped}}^{(\text{SD,amp})}(N, P) = \frac{P}{N + 2}. \quad (50)$$

The reference shaping region is a hypercube in electric field magnitude. This region is equivalently described as the set of signal points with a peak power constraint A on each constituent 1-D symbol:

$$\mathcal{R}_{\text{ref}}^{(\text{SD,amp})}(N, A) = \left\{ \mathbf{X} \in \mathbb{R}_+^N \mid \|\mathbf{X}\|_\infty \leq A \right\}. \quad (51)$$

The volume of the shaping region is

$$\mathcal{V}_{\text{ref}}^{(\text{SD,amp})}(N, A) = A^N. \quad (52)$$

The average optical power of the shaping region is the second moment of the electric field magnitude in any one dimension,

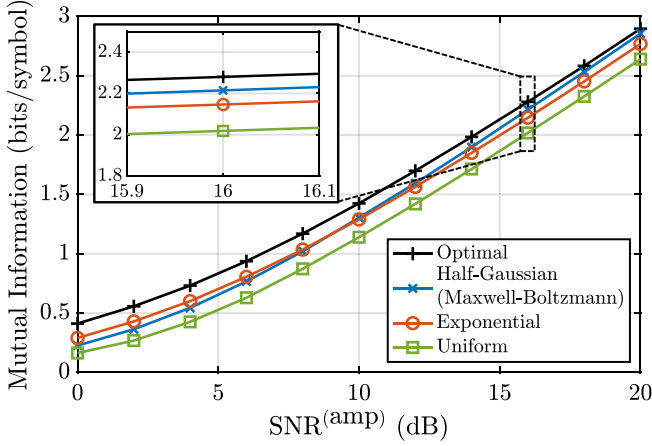


Fig. 12. Mutual information vs. $\text{SNR}^{(\text{amp})}$ for amplifier noise-limited SD detection. The 128-point constellations are uniformly spaced in electric field magnitude. Adapted from [45].

and is given by

$$\bar{P}_{\text{ref}}^{(\text{SD,amp})}(A) = \frac{A^2}{3}. \quad (53)$$

3) *Induced Distribution and Shaping Gain:* The induced density in one basic dimension must satisfy the following [34]:

$$f_{X_1}(N, P, x) \propto \left(1 - \frac{x^2}{(N+2)\bar{P}_{\text{shaped}}^{(\text{SD,amp})}(N, P)}\right)^{\frac{N-1}{2}}, \quad (54)$$

$$x \in [0, \sqrt{P}].$$

Substituting $\mathbb{E}[X_1^2] = \bar{P}_{\text{shaped}}^{(\text{SD,amp})}(N, P)$ into (54) and taking the limit as $N \rightarrow \infty$, we get

$$f_{X_1}(x) \triangleq \lim_{N \rightarrow \infty} f_{X_1}(N, P, x) \propto \exp\left(-\frac{1}{2} \frac{x^2}{\mathbb{E}[X_1^2]}\right), \quad x \in \mathbb{R}_+. \quad (55)$$

The optimal shaping region for the amplifier noise-limited SD receiver induces an MB distribution in electric field magnitude. We note that a half-Gaussian distribution in the electric field magnitude corresponds to a Gamma distribution with shape parameter $k = 1/2$ and scale parameter $\theta = 2\bar{P}$ in the intensity.

To compute the ultimate shaping gain for amplifier noise-limited SD detection, we must equate the volumes in (49) and (52). Equating the volumes yields a relationship between P and A and using Stirling's approximation, the ultimate shaping gain is the ratio of (50) and (53) as $N \rightarrow \infty$, and is given by

$$\gamma_s^{(\text{SD,amp})} = \lim_{N \rightarrow \infty} \frac{\bar{P}_{\text{ref}}^{(\text{SD,amp})}(A)}{\bar{P}_{\text{shaped}}^{(\text{SD,amp})}(N, P)} = \frac{\pi e}{6}. \quad (56)$$

Fig. 12 shows the mutual information vs. $\text{SNR}^{(\text{amp})}$ for amplifier noise-limited SD detection using 128-point constellations uniformly spaced in electric field magnitude with optimal, MB, exponential, and uniform input distributions. The optimal distribution and its mutual information are computed numerically using the BA method, as explained in Section III-D. For

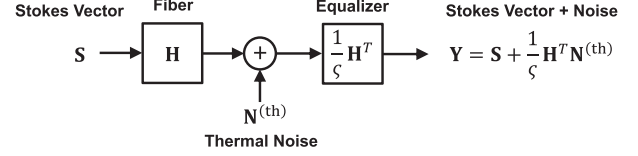


Fig. 13. Discrete-time channel model for SV detection in the thermal noise-limited regime. The noise covariance matrix $\text{cov}\{\frac{1}{\zeta}\mathbf{H}^T\mathbf{N}^{(\text{th})}\}$ is independent of the transmitted SV \mathbf{S} . Adapted from [45].

$\text{SNR}^{(\text{amp})} < 8$ dB, an exponential distribution in electric field magnitude outperforms the MB distribution. For $\text{SNR}^{(\text{amp})} > 10$ dB, the MB distribution in electric field magnitude outperforms the exponential distribution. As $\text{SNR}^{(\text{amp})}$ increases from 10 dB to 20 dB, the mutual information achieved by the MB distribution converges to that achieved by the optimal distribution. These results are consistent with the HCA derivation, which states that a half-Gaussian distribution in electric field magnitude is the optimal distribution at high SNR.

The shaping gain achieved by the optimal distribution over the uniform distribution depends on the target mutual information. At 0.5 bits/symbol, the shaping gain of the optimal distribution over the uniform distribution is greater than 3 dB. At 2.5 bits/symbol, the shaping gain of the optimal distribution is about 1.5 dB, in agreement with the analytical result (56), i.e., $\pi e/6 \approx 1.53$ dB.

For simplicity, we have assumed both the signal and ASE noise are received in only one polarization, since the dominant signal-ASE beat noise arises only from the noise that is co-polarized with the signal. If the receiver were to also detect ASE noise in the orthogonal polarization, it would affect only the ASE-ASE beat noise. This would not change the input distribution found using HCA, but would slightly degrade the performance obtained using any input distribution at low values of $\text{SNR}^{(\text{amp})}$.

D. Stokes Vector Detection, Thermal Noise-Limited

In this subsection, we review the application of HCA to thermal noise-limited SV detection [35]. We consider the specific SV receiver structures shown in [22, Fig. 3] and [23, Fig. 1(a)], which yield identical outputs in principle. These structures may be considered canonical because they directly yield the three components of the received Stokes vector with identical signal gains and noise distributions, and because they minimize the number of required electrical outputs and analog-to-digital converters.

The discrete-time channel model for thermal noise-limited SV detection is shown in Fig. 13 and given by

$$\mathbf{Y} = \frac{1}{\zeta}\mathbf{H}^T(\mathbf{H}\mathbf{S} + \mathbf{N}^{(\text{th})}) = \mathbf{S} + \frac{1}{\zeta}\mathbf{H}^T\mathbf{N}^{(\text{th})}. \quad (57)$$

Here, \mathbf{H} is a 3×3 real orthogonal Mueller matrix with channel gain $\mathbf{H}^T\mathbf{H} = \zeta\mathbf{I}_3$, $\mathbf{S} = [S_1, S_2, S_3]^T$ is the SV of the transmitted electric field, and $\mathbf{N}^{(\text{th})} = [N_1^{(\text{th})}, N_2^{(\text{th})}, N_3^{(\text{th})}]^T$ is a jointly Gaussian AWGN vector with covariance matrix $\text{cov}\{\mathbf{N}^{(\text{th})}\} = \sigma_n^2\mathbf{I}_3$.

The discrete-time model presumes the channel is known at the receiver and that the receiver uses memoryless digital signal processing to compensate for the effects of the channel. The covariance of the noise after the signal processing is an IID jointly Gaussian AWGN vector because the covariance matrix is

$$\text{cov} \left\{ \frac{1}{\varsigma} \mathbf{H}^T \mathbf{N}^{(\text{th})} \right\} = \frac{1}{\varsigma} \sigma_{\text{th}}^2 \mathbf{I}_3. \quad (58)$$

1) *Natural Coordinates*: Consider two arbitrary SVs \mathbf{S}_1 and \mathbf{S}_2 input into the channel. Under ML detection, the pairwise error probability is

$$P_e(\mathbf{S}_1, \mathbf{S}_2) = Q \left(\frac{\|\mathbf{S}_1 - \mathbf{S}_2\|_2}{2\sigma_{\text{th}}} \right). \quad (59)$$

We therefore conclude that the Stokes parameters are the natural coordinates for thermal noise-limited SV detection.

2) *Shaping Regions*: Let $\mathbf{S}^{(N)} = [\mathbf{S}_1^T, \mathbf{S}_2^T, \dots, \mathbf{S}_N^T]^T = [S_{1,1}, S_{1,2}, S_{1,3}, S_{2,1}, \dots, S_{N,3}]$ be a length- $3N$ real vector of Stokes parameters formed by concatenating N 3-D SVs in N disjoint symbol intervals. The average optical power is

$$\frac{1}{N} \mathbf{S}_0^{(N)} = \frac{1}{N} \left\| \mathbf{S}^{(N)} \right\|_2 = \frac{1}{N} \sum_{i=1}^N \|\mathbf{S}_i\|_2. \quad (60)$$

The optimal shaping region is the set of $3N$ -D signal points with the property that the sum of the optical powers of the N constituent 3-D SVs is less than or equal to the total power P . It is defined by

$$\mathcal{R}_{\text{shaped}}^{(\text{SV,th})}(N, P) = \left\{ \mathbf{S}^{(N)} \in \mathbb{R}^{3N} \mid \sum_{i=1}^N S_{i,0} \leq P \right\} \quad (61)$$

$$= \left\{ \mathbf{S}^{(N)} \in \mathbb{R}^{3N} \mid \sum_{i=1}^N \|\mathbf{S}_i\|_2 \leq P \right\}. \quad (62)$$

Fig. 14(a) shows the optimal shaping region for thermal noise-limited SV detection for $N = 2$, which is a 2-D simplex. It corresponds to the shaping region $\mathcal{R}_{\text{shaped}}^{(\text{SV,th})}(2, P)$ given in (61), which is an L_1 -norm constraint on the zeroth Stokes parameter. A 6-D signal point $\mathbf{S}^{(2)} = [\mathbf{S}_1^T, \mathbf{S}_2^T]^T$ is specified by indicating the values of the two constituent 3-D signal points \mathbf{S}_1 and \mathbf{S}_2 . The black dot indicates the 2-D coordinates of the corresponding zeroth Stokes parameters, which are $\|\mathbf{S}_1\|_2 = S_{1,0}$ and $\|\mathbf{S}_2\|_2 = S_{2,0}$, respectively. Fig. 14(b) contains two shaded 3-D balls enclosed by two outer balls with radius P , which is an alternative method of depicting $\mathbf{S}^{(2)}$. The coordinates on the left and right shaded 3-D balls are $\mathbf{S}_1 = \{S_{1,1}, S_{1,2}, S_{1,3}\}$ and $\mathbf{S}_2 = \{S_{2,1}, S_{2,2}, S_{2,3}\}$, respectively, which are indicated by the black dots. The radii of the shaded 3-D balls are $S_{1,0}$ and $S_{2,0}$, respectively. Any pair of 3-D signal points that lie on the surfaces of the shaded 3-D balls in Fig. 14(b) map back to $\mathbf{S}^{(2)}$ in Fig. 14(a).

Let $\mathcal{V}_{\text{shaped}}^{(\text{SV,th})}(N, P)$ be the volume of $\mathcal{R}_{\text{shaped}}^{(\text{SV,th})}(N, P)$. A closed-form expression for $\mathcal{V}_{\text{shaped}}^{(\text{SV,th})}(N, P)$ is [35]:

$$\mathcal{V}_{\text{shaped}}^{(\text{SV,th})}(N, P) = P^{3N} \frac{(8\pi)^N}{\Gamma(3N + 1)}. \quad (63)$$

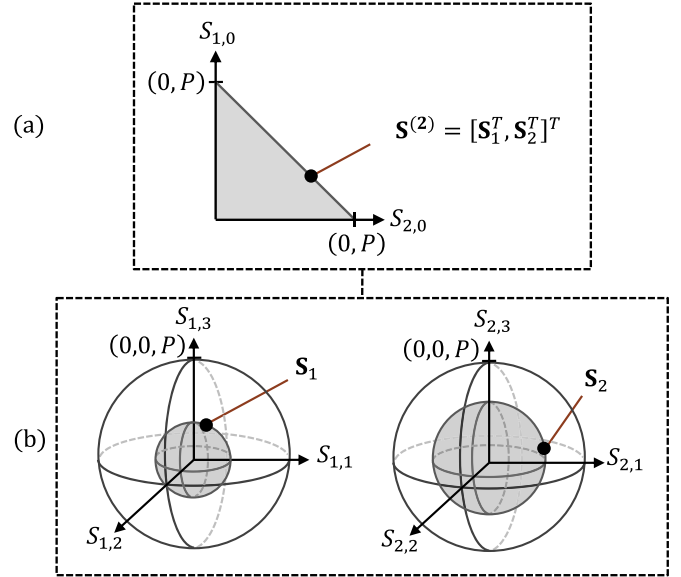


Fig. 14. (a) Optimal shaping region for thermal noise-limited SV detection for $N = 2$ Stokes symbols \mathbf{S}_1 and \mathbf{S}_2 . The figure depicts the 6-D real vector $\mathbf{S}^{(2)}$ in terms of $S_{1,0}$ and $S_{2,0}$, the zeroth Stokes parameters of \mathbf{S}_1 and \mathbf{S}_2 , respectively. $\mathbf{S}^{(2)}$ is a signal point on the surface of $\mathcal{R}_{\text{shaped}}^{(\text{SV,th})}(2, P)$, which is a 2-simplex in S_0 . The maximum- L_1 -norm constraint on the simplex is P . (b) \mathbf{S}_1 and \mathbf{S}_2 shown on separate 3-D plots with the individual Stokes parameters $\{S_{1,1}, S_{1,2}, S_{1,3}\}$ and $\{S_{2,1}, S_{2,2}, S_{2,3}\}$ as coordinates. The radii of the outer 3-D balls are also P .

The average optical power of the region $\mathcal{R}_{\text{shaped}}^{(\text{SV,th})}(N, P)$ is

$$\bar{P}_{\text{shaped}}^{(\text{SV,th})}(N, P) = \frac{3}{3N + 1} P. \quad (64)$$

The reference shaping region is a hypercube in Stokes space, and can be described by the set of signal points with maximum- L_∞ -norm constraint A . The analytical form for $\mathcal{R}_{\text{ref}}^{(\text{SV,th})}(N, A)$ is given by

$$\mathcal{R}_{\text{ref}}^{(\text{SV,th})}(N, A) = \left\{ \mathbf{S}^{(N)} \in \mathbb{R}^{3N} \mid \left\| \mathbf{S}^{(N)} \right\|_\infty \leq A \right\}. \quad (65)$$

The volume of $\mathcal{R}_{\text{ref}}^{(\text{SV,th})}(N, A)$ is

$$\mathcal{V}_{\text{ref}}^{(\text{SV,th})}(N, A) = (2A)^{3N}. \quad (66)$$

By symmetry, we can compute the average optical power by considering only \mathbf{S}_1 . For the reference shaping region, $S_{1,1}, S_{1,2}$, and $S_{1,3}$ are mutually independent and uniformly distributed from $[-A, A]$. The average optical power per Stokes symbol is

$$\bar{P}_{\text{ref}}^{(\text{SV,th})}(A) = \mathbb{E} \left[\sqrt{S_{1,1}^2 + S_{1,2}^2 + S_{1,3}^2} \right] \quad (67)$$

$$\approx 0.961A \quad (68)$$

$$\leq A. \quad (69)$$

Eq. (68) comes from numerically approximating (67) and (69) follows from Jensen's inequality, and is an upper bound of the exact expression (67).

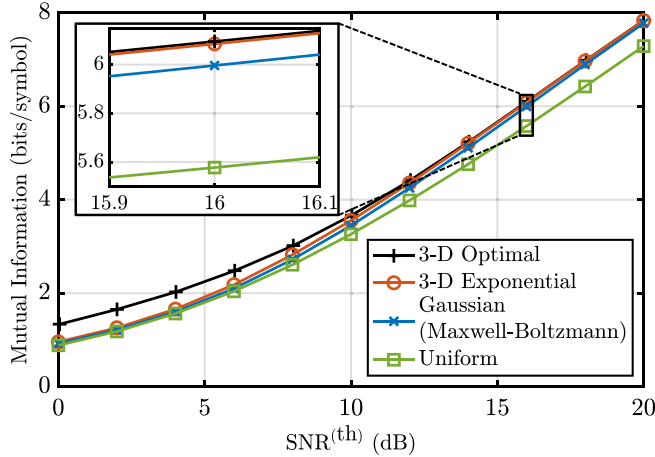


Fig. 15. Mutual information vs. $\text{SNR}^{(\text{th})}$ for thermal noise-limited SV detection. The $(12 \times 12 \times 12)$ constellations are uniformly spaced in Stokes space.

3) *Induced Distribution and Shaping Gain:* The induced density in one basic dimension must satisfy the following [35]:

$$f_{\mathbf{s}_1}(N, P, \mathbf{s}) \propto \left(1 - \frac{3 \|\mathbf{s}\|_2}{(3N+1)\bar{P}_{\text{shaped}}^{(\text{SV}, \text{th})}(N, P)}\right)^{3N-3},$$

$$\|\mathbf{s}\|_2 \in [0, P]. \quad (70)$$

Setting the average power to a constant $\bar{P}_{\text{shaped}}^{(\text{SV}, \text{th})}(N, P) = \bar{P}$, and taking the limit as $N \rightarrow \infty$, we obtain

$$f_{\mathbf{s}_1}(\mathbf{s}) = \lim_{N \rightarrow \infty} f_{\mathbf{s}_1}(N, \mathbf{s})$$

$$\propto \exp\left(\frac{-\|\mathbf{s}\|_2}{\bar{P}/3}\right), \|\mathbf{s}\|_2 \in \mathbb{R}_+. \quad (71)$$

Normalizing the density, we get

$$f_{\mathbf{s}_1}(\mathbf{s}) = \frac{1}{8\pi} \left(\frac{1}{\bar{P}/3}\right)^3 \exp\left(\frac{-\|\mathbf{s}\|_2}{\bar{P}/3}\right), \|\mathbf{s}\|_2 \in \mathbb{R}_+. \quad (72)$$

We conclude that the optimal input distribution for the thermal noise-limited SVR is a 3-D exponential distribution in S_0 .

Computing the ultimate shaping gain of thermal noise-limited SV detection requires equating the volumes in (63) and (66). Taking the ratio of $\bar{P}_{\text{ref}}^{(\text{SV}, \text{th})}(A)$ to $\bar{P}_{\text{shaped}}^{(\text{SV}, \text{th})}(N, P)$ as $N \rightarrow \infty$ with volumes equated, we find

$$\gamma_s^{(\text{SV}, \text{th})} = \lim_{N \rightarrow \infty} \frac{\bar{P}_{\text{ref}}^{(\text{SV}, \text{th})}(A)}{\bar{P}_{\text{shaped}}^{(\text{SV}, \text{th})}(N, P)} \quad (73)$$

$$\approx 0.961 \frac{\sqrt[3]{\pi e}}{3} \approx 1.056 \text{ dB} \quad (74)$$

$$\leq \frac{\sqrt[3]{\pi e}}{3} \approx 1.23 \text{ dB}. \quad (75)$$

Eq. (74) uses the approximation in (68), and (75) uses the upper bound (69).

Fig. 15 shows the mutual information vs. $\text{SNR}^{(\text{th})}$ for the 3-D optimal distribution, 3-D exponential distribution, 3-D MB, and uniform distribution. The $(12 \times 12 \times 12)$ constellations are

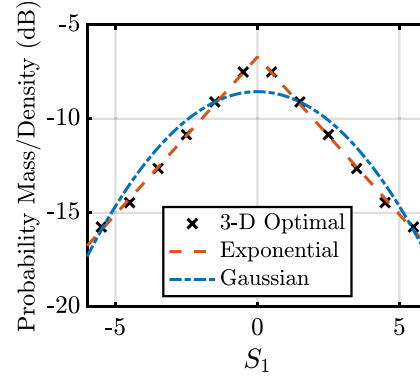


Fig. 16. 3-D optimal distribution vs. S_1 for $S_2 = S_3 = 0.5$ and $\text{SNR}^{(\text{th})} = 20$ dB for thermal noise-limited SV detection computed using the BA algorithm. The unnormalized continuous exponential and Gaussian densities are fitted to minimize the L_1 -norm of the fitting error in dB.

uniformly spaced in Stokes space, and the input distributions and thermal noise standard deviation σ_{th} are optimized using the methods described in Section III-D. The 3-D exponential distribution outperforms the MB distribution over the entire range of $\text{SNR}^{(\text{th})}$ studied, while both distributions outperform the uniform distribution over the entire range of $\text{SNR}^{(\text{th})}$ studied. The 3-D exponential distribution is within 0.01 bits/symbol of the 3-D optimal distribution at $\text{SNR}^{(\text{th})} = 16$ dB.

The shaping gain of the 3-D optimal distribution over the uniform distribution at 6.4 bits/symbol is 1.25 dB. This is almost 0.15 dB higher than the 1.105 dB shaping gain estimated using the $(8 \times 8 \times 8)$ constellation in [35]. This higher shaping gain is a consequence of the larger $(12 \times 12 \times 12)$ constellation used in Fig. 15. The ultimate shaping gain derived in (74) is 2.11 dB when expressed in terms of $\text{SNR}^{(\text{th})}$, indicating that our numerical simulation achieves roughly 60% of the ultimate shaping gain. In Fig. 6, we showed that SC detection achieves roughly 65% of the ultimate shaping gain when using $M = 256$, which uses 16 constellation points per signaling dimension. The gap to the maximum theoretical shaping gain is similar for SC detection and thermal noise-limited SV detection. The gap between the theoretical maximum and numerically estimated shaping gains can be reduced by using 3-D constellations with more signal points.

Fig. 16 shows the 3-D optimal distribution vs. S_1 for $S_2 = S_3 = 0.5$ and $\text{SNR}^{(\text{th})} = 20$ dB computed using the BA algorithm. The continuous exponential and Gaussian distributions are fitted to minimize the L_1 -norm of the fitting error in dB. The exponential better fits the 3-D optimal distribution than the Gaussian does. This result is consistent with the 3-D exponential distribution analytically derived in (72) for thermal noise-limited SV detection.

E. Stokes Vector Detection, Amplifier Noise-Limited

In this subsection, we review the application of HCA to amplifier noise-limited SV detection [35]. As in the previous subsection, we consider the specific SV receiver structures shown in [22, Fig. 3] and [23, Fig. 1(a)], which may be considered canonical.

We first state the discrete-time channel model in terms of electric field components and then derive the discrete-time channel model in terms of Stokes vector components. A received electric field vector \mathbf{E}_R is

$$\mathbf{E}_R = \mathbf{E}' + \mathbf{N}^{(\text{amp})}, \quad (76)$$

where $\mathbf{E} = [E_1, E_2]^T = [E_{1I} + jE_{1Q}, E_{2I} + jE_{2Q}]^T$ is the transmitted electric field, \mathbf{U} is a scaled unitary matrix satisfying $\mathbf{U}\mathbf{U}^H = \sqrt{\varsigma}\mathbf{I}_2$, $\mathbf{E}' = \mathbf{U}\mathbf{E} = [E'_{1I} + jE'_{1Q}, E'_{2I} + jE'_{2Q}]^T$ is the electric field after multiplication by \mathbf{U} , and $\mathbf{N}^{(\text{amp})} = [N_1^{(\text{amp})}, N_2^{(\text{amp})}]^T = [N_{1I} + jN_{1Q}, N_{2I} + jN_{2Q}]^T$ is a complex, circularly symmetric jointly Gaussian AWGN vector with covariance matrix $\text{cov}\{\mathbf{N}^{(\text{amp})}\} = 2\sigma_{\text{amp}}^2\mathbf{I}_2$.

Let \mathbf{S} be the SV corresponding to the electric field vector \mathbf{E} . After detection and MIMO equalization, the detected electrical signals are

$$\mathbf{Y} = \mathbf{S} + \frac{1}{\varsigma}\mathbf{H}^T\tilde{\mathbf{N}}^{(\text{amp})}. \quad (77)$$

The channel matrix \mathbf{U} transforms to an orthogonal Mueller matrix \mathbf{H} with $\mathbf{H}^T\mathbf{H} = \varsigma\mathbf{I}_3$ [51]. The real noise vector $\tilde{\mathbf{N}}^{(\text{amp})} = [\tilde{N}_1^{(\text{amp})}, \tilde{N}_2^{(\text{amp})}, \tilde{N}_3^{(\text{amp})}]^T$ has components

$$\begin{aligned} \tilde{N}_1^{(\text{amp})} &= 2N_{1I}E'_{1I} + 2N_{1Q}E'_{1Q} - 2N_{2I}E'_{2I} \\ &\quad - 2N_{2Q}E'_{2I} + N_{1I}^2 + N_{1Q}^2 - N_{2I}^2 - N_{2Q}^2, \end{aligned} \quad (78)$$

$$\begin{aligned} \tilde{N}_2^{(\text{amp})} &= 2N_{1I}E'_{2I} + 2N_{1Q}E'_{2Q} + 2N_{2I}E'_{1I} \\ &\quad + 2N_{2Q}E'_{1Q} + 2N_{1I}N_{2I} + 2N_{1Q}N_{2Q}, \end{aligned} \quad (79)$$

$$\begin{aligned} \tilde{N}_3^{(\text{amp})} &= -2N_{1I}E'_{2Q} + 2N_{1Q}E'_{2I} + 2N_{2I}E'_{1Q} \\ &\quad - 2N_{2Q}E'_{1I} + 2N_{1Q}N_{2I} - 2N_{1I}N_{2Q}. \end{aligned} \quad (80)$$

As in Section IV-C, we derive an approximate channel model that neglects ASE-ASE beat noise. Let $\tilde{\mathbf{N}}^{(\text{amp})} = [\tilde{N}_1^{(\text{amp})}, \tilde{N}_2^{(\text{amp})}, \tilde{N}_3^{(\text{amp})}]^T$ be the noise vector obtained by dropping all ASE-ASE beat noise terms from $\tilde{\mathbf{N}}^{(\text{amp})}$, which has components

$$\begin{aligned} \tilde{N}_1^{(\text{amp})} &= 2N_{1I}E'_{1I} + 2N_{1Q}E'_{1Q} - 2N_{2I}E'_{2I} \\ &\quad - 2N_{2Q}E'_{2I}, \end{aligned} \quad (81)$$

$$\begin{aligned} \tilde{N}_2^{(\text{amp})} &= 2N_{1I}E'_{2I} + 2N_{1Q}E'_{2Q} + 2N_{2I}E'_{1I} \\ &\quad + 2N_{2Q}E'_{1Q}, \end{aligned} \quad (82)$$

$$\begin{aligned} \tilde{N}_3^{(\text{amp})} &= -2N_{1I}E'_{2Q} + 2N_{1Q}E'_{2I} + 2N_{2I}E'_{1Q} \\ &\quad - 2N_{2Q}E'_{1I}. \end{aligned} \quad (83)$$

Substituting in $\tilde{\mathbf{N}}^{(\text{amp})}$ for $\tilde{\mathbf{N}}^{(\text{amp})}$ in (77), we obtain

$$\mathbf{Y} \approx \mathbf{S} + \frac{1}{\varsigma}\mathbf{H}^T\tilde{\mathbf{N}}^{(\text{amp})}. \quad (84)$$

The approximate channel model (84) is depicted in Fig. 17.

In the HCA derivation of the optimal shaping distribution, we use the approximate channel model (84), setting $\varsigma = 1$. In numerical simulations to evaluate mutual information, we use

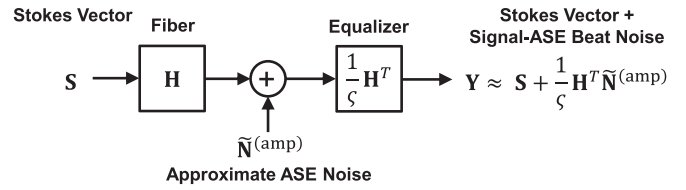


Fig. 17. Discrete-time channel model for SV detection in the amplifier noise-limited regime. The approximation, made at high signal-to-noise ratio, neglects ASE-ASE beat noise. The signal-ASE beat noise covariance matrix $\text{cov}\{\frac{1}{\varsigma}\mathbf{H}^T\tilde{\mathbf{N}}^{(\text{amp})}\}$ scales linearly with the signal energy $\|\mathbf{S}\|_2$. ASE: Amplified spontaneous emission. Adapted from [45].

the exact channel model (77), which includes both signal-ASE and ASE-ASE beat noises.

1) *Natural Coordinates*: Consider two arbitrary SVs \mathbf{S}_1 and \mathbf{S}_2 input to the channel described by (84). To derive an expression for the error probability for arbitrary \mathbf{S}_1 and \mathbf{S}_2 , we assume that a normalized correlation detector computes an inner product between the detected electrical currents \mathbf{Y} and the vector $(\mathbf{S}_1 - \mathbf{S}_2)/\|\mathbf{S}_1 - \mathbf{S}_2\|_2$ to form a decision statistic [52, Ch. 4.3]. The decoding rule using a decision threshold Y_d is

$$\mathbf{Y}^T \frac{\mathbf{S}_1 - \mathbf{S}_2}{\|\mathbf{S}_1 - \mathbf{S}_2\|_2} \stackrel{\text{S}}{\underset{\text{S}_2}{\gtrless}} Y_d. \quad (85)$$

The ML decision threshold, which minimizes the error probability, is well approximated by

$$Y_d = \frac{\|\mathbf{S}_2\|_2^{1/2} \left(\mathbf{S}_2^T \mathbf{S}_1 - \|\mathbf{S}_1\|_2^2 \right) + \|\mathbf{S}_1\|_2^{1/2} \left(\|\mathbf{S}_2\|_2^2 - \mathbf{S}_1^T \mathbf{S}_2 \right)}{\|\mathbf{S}_1 - \mathbf{S}_2\|_2 \left(\|\mathbf{S}_1\|_2^{1/2} + \|\mathbf{S}_2\|_2^{1/2} \right)}. \quad (86)$$

Let $P_e(\mathbf{S}_i|\mathbf{S}_j)$ be the conditional error probability of decoding \mathbf{S}_i when \mathbf{S}_j is transmitted. Assuming the channel is exactly described by (84), the approximate ML decision threshold (86) results in $P_e(\mathbf{S}_1|\mathbf{S}_2) = P_e(\mathbf{S}_2|\mathbf{S}_1) = P_e(\mathbf{S}_1, \mathbf{S}_2)$, which is given by

$$P_e(\mathbf{S}_1, \mathbf{S}_2) = Q \left(\frac{\|\mathbf{S}_1 - \mathbf{S}_2\|_2}{2\sigma_{\text{amp}}(\|\mathbf{S}_1\|_2^{1/2} + \|\mathbf{S}_2\|_2^{1/2})} \right). \quad (87)$$

We now introduce an invertible transformation from Stokes space to scaled Stokes space to aid in simplifying (87). Let $\mathbf{X} = [X_1, X_2, X_3]$ be a 3-D scaled Stokes symbol, where X_1, X_2, X_3 are the corresponding scaled Stokes parameters. The zeroth scaled Stokes parameter is $X_0 = \|\mathbf{X}\|_2$. \mathbf{X} is defined in terms of \mathbf{S} by

$$[X_1, X_2, X_3]^T = \frac{[S_1, S_2, S_3]^T}{\sqrt{S_0}} = \frac{[S_1, S_2, S_3]^T}{\sqrt{S_1^2 + S_2^2 + S_3^2}}. \quad (88)$$

To simplify (87), we make the approximation that $\|\mathbf{S}_1\|_2^{1/2} \approx \|\mathbf{S}_2\|_2^{1/2}$. Using this approximation, we obtain

$$\begin{aligned} P_e(\mathbf{S}_1, \mathbf{S}_2) &\approx Q \left(\frac{1}{4\sigma_{\text{amp}}} \left\| \frac{\mathbf{S}_1}{\|\mathbf{S}_1\|_2^{1/2}} - \frac{\mathbf{S}_2}{\|\mathbf{S}_2\|_2^{1/2}} \right\|_2 \right) \\ &= Q \left(\frac{1}{4\sigma_{\text{amp}}} \|\mathbf{X}_1 - \mathbf{X}_2\|_2 \right). \end{aligned} \quad (89)$$

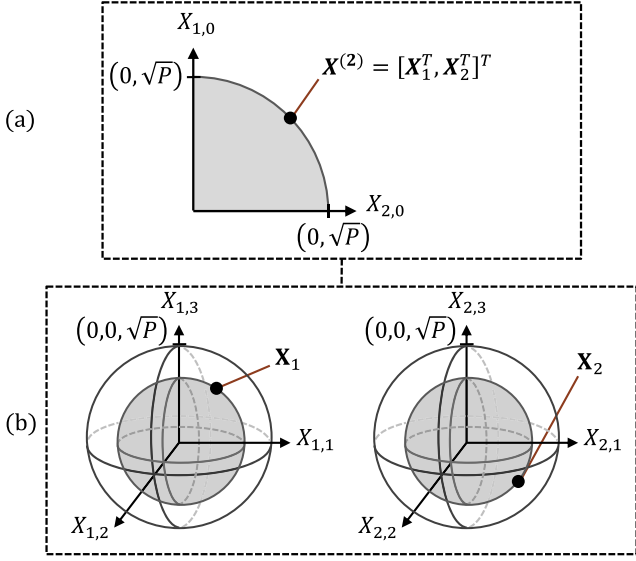


Fig. 18. (a) Optimal shaping region for amplifier noise-limited SV detection for $N = 2$. The figure depicts a 6-D real vector $\mathbf{X}^{(2)}$ in terms of $X_{1,0}$ and $X_{2,0}$, the zeroth scaled Stokes parameters of \mathbf{X}_1 and \mathbf{X}_2 , respectively. $\mathbf{X}^{(2)}$ is a signal point on the surface of $\mathcal{R}_{\text{shaped}}^{(\text{SV,amp})}(2, P)$, which is a 2-ball in X_0 with radius \sqrt{P} intersected with the non-negative orthant. (b) \mathbf{X}_1 and \mathbf{X}_2 shown on separate 3-D plots with scaled Stokes parameters $\{X_{1,1}, X_{1,2}, X_{1,3}\}$ and $\{X_{2,1}, X_{2,2}, X_{2,3}\}$ as coordinates. The radii of the outer 3-D balls in the bottom plot are also equal to \sqrt{P} .

Since the pairwise error probability is expressed as a Q-function of the L_2 -norm of the difference between scaled Stokes vectors, we conclude that the scaled Stokes parameters are natural coordinates for amplifier noise-limited SV detection.

2) *Shaping Regions*: Let $\mathbf{X}^{(N)} = [\mathbf{X}_1^T, \mathbf{X}_2^T, \dots, \mathbf{X}_N^T]^T = [X_{1,1}, X_{1,2}, X_{1,3}, X_{2,1}, \dots, X_{N,3}]$ be a length- $3N$ real vector of scaled Stokes parameters that is formed by concatenating N 3-D scaled SVs in N disjoint symbol intervals. The average optical power of $\mathbf{X}^{(N)}$ is

$$\frac{1}{N} \|\mathbf{X}^{(N)}\|_2^2 = \frac{1}{N} \sum_{i=1}^N \|\mathbf{X}_i\|_2^2. \quad (90)$$

The optimal shaping region is the set of $3N$ -D signal points with total optical power less than or equal to the maximum optical power constraint P . The optimal shaping region is described by

$$\mathcal{R}_{\text{shaped}}^{(\text{SV,amp})}(N, P) = \left\{ \mathbf{X}^{(N)} \in \mathbb{R}^{3N} \mid \sum_{i=1}^N \|\mathbf{X}_i\|_2^2 = P \right\}. \quad (91)$$

Fig. 18(a) shows the optimal shaping region for $N = 2$. A 2-D representation of the 6-D shaping region $\mathcal{R}_{\text{shaped}}^{(\text{SV,amp})}(N, P)$ is a disk with radius \sqrt{P} intersected with the nonnegative orthant. The coordinates are the zeroth scaled Stokes parameters $\|\mathbf{X}_1\|_2 = X_{1,0}$ and $\|\mathbf{X}_2\|_2 = X_{2,0}$, respectively. The real 6-D vector $\mathbf{X}^{(2)}$ is a signal point on the surface of $\mathcal{R}_{\text{shaped}}^{(\text{SV,amp})}(N, P)$. It is indicated using a black dot in Fig. 18(a). Fig. 18(b) shows an alternative method of describing the real 6-D vector $\mathbf{X}^{(2)}$. The coordinates on the left and right shaded 3-D balls are $\mathbf{X}_1 =$

$\{X_{1,1}, X_{1,2}, X_{1,3}\}$ and $\mathbf{X}_2 = \{X_{2,1}, X_{2,2}, X_{2,3}\}$, respectively, which are indicated by the black dots. The radii of both outer balls are \sqrt{P} . The radii of the shaded 3-D balls are $X_{1,0}$ and $X_{2,0}$, respectively. Pairs of 3-D signal points that lie on the surfaces of the two shaded 3-D balls in Fig. 18(b) map to $\mathbf{X}^{(2)}$ in Fig. 18(a).

It is worth noting that a $3N$ -D ball in scaled Stokes space with radius \sqrt{P} maps to a $3N$ -D ball in Stokes space with radius P via the transformation in (88). However, a uniform distribution of signal points in scaled Stokes space does not map to a uniform distribution of signal points in Stokes space because of the Jacobian of the transformation (88). Computations of the volume and average power in HCA must be done using the natural coordinates.

The volume of the region $\mathcal{R}_{\text{shaped}}^{(\text{SV,amp})}(N, P)$ is the volume of a $3N$ -D ball with radius \sqrt{P} , and is given by

$$\mathcal{V}_{\text{shaped}}^{(\text{SV,amp})}(N, P) = \frac{(\pi P)^{3N/2}}{\Gamma(\frac{3N}{2} + 1)}. \quad (92)$$

The average optical power of the region $\mathcal{R}_{\text{shaped}}^{(\text{SV,amp})}(N, P)$ is

$$\bar{P}_{\text{shaped}}^{(\text{SV,amp})}(N, P) = \frac{3P}{3N + 2}. \quad (93)$$

The reference shaping region is a hypercube in scaled Stokes space. The analytical form for $\mathcal{R}_{\text{ref}}^{(\text{SV,amp})}(N, A)$ is given by

$$\mathcal{R}_{\text{ref}}^{(\text{SV,amp})}(N, A) = \left\{ \mathbf{X}^{(N)} \in \mathbb{R}^{3N} \mid \|\mathbf{X}^{(N)}\|_{\infty} \leq A \right\}, \quad (94)$$

where A is the L_{∞} -norm constraint in scaled Stokes space. The volume of the region is

$$\mathcal{V}_{\text{ref}}^{(\text{SV,amp})}(N, A) = (2A)^{3N}. \quad (95)$$

By symmetry, the average optical power is $\bar{P}_{\text{ref}}^{(\text{SV,amp})}(A) = \mathbb{E}[\|\mathbf{X}_1\|_2^2]$ for any N . Computing the average second moment of \mathbf{X}_1 , we obtain

$$\bar{P}_{\text{ref}}^{(\text{SV,amp})}(A) = A^2. \quad (96)$$

3) *Induced Distribution and Shaping Gain*: In Section III-C, we showed that an N -D complex ball induces a complex circularly symmetric Gaussian distribution in one complex dimension as $N \rightarrow \infty$. In Section IV-C, we also showed that an N -D real ball intersected with the nonnegative orthant induces a half-Gaussian distribution in one real dimension. Using an almost identical proof, it is straightforward to show that the distribution induced in \mathbf{X} is a 3-D IID real Gaussian distribution. The PDF of $\mathbf{X} \sim \mathcal{N}(0, \sigma^2 \mathbf{I}_3)$ is given by

$$f_{\mathbf{X}}(\mathbf{x}) = \frac{1}{(2\pi\sigma^2)^{3/2}} \exp\left(-\frac{1}{2\sigma^2} \|\mathbf{x}\|_2^2\right), \quad (97)$$

where $\sigma^2 = \bar{P}/3$ is the input power constraint on each real dimension of \mathbf{X} .

The induced density in Stokes space is given by the following [35]:

$$f_{\mathbf{s}}(\mathbf{s}) = \frac{1}{2\|\mathbf{s}\|_2^{3/2}} \frac{1}{(2\pi\bar{P}/3)^{3/2}} \exp\left(-\frac{1}{2} \frac{1}{\bar{P}/3} \|\mathbf{s}\|_2\right). \quad (98)$$

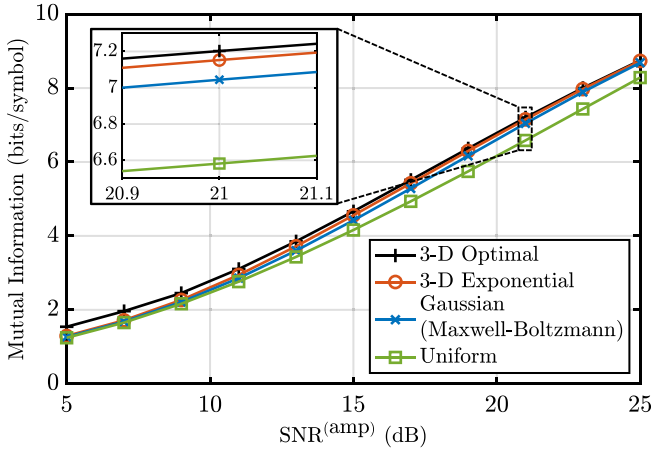


Fig. 19. Mutual information (MI) vs. $\text{SNR}^{(\text{amp})}$ for amplifier noise-limited SV detection. The $(12 \times 12 \times 12)$ constellations are uniformly spaced in Stokes space.

The distribution of \mathbf{S} , given by (98), is undefined at $\mathbf{s} = 0$. However, (98) is only a function of $\|\mathbf{s}\|_2 = s_0$. We can write the distribution induced in S_0 as

$$f_{S_0}(s_0) = 2\pi s_0^{1/2} \frac{1}{(2\pi \bar{P}/3)^{3/2}} \exp\left(-\frac{1}{2} \frac{1}{\bar{P}/3} s_0\right). \quad (99)$$

From (99), we can see that $S_0 \sim \text{Gamma}(3/2, 2\bar{P}/3)$, i.e., S_0 is Gamma distributed with shape parameter $k = 3/2$ and scale parameter $\theta = 2\bar{P}/3$. While the distribution of \mathbf{S} is undefined at $\mathbf{s} = 0$, the distribution of S_0 is well defined at $s_0 = 0$.

To compute the ultimate shaping gain for amplifier noise-limited SV detection, we equate the volumes in (92) and (95). Using Stirling's approximation, we find that

$$\gamma_s^{(\text{SV,amp})} = \lim_{N \rightarrow \infty} \frac{\bar{P}_{\text{ref}}^{(\text{SV,amp})}(A)}{\bar{P}_{\text{shaped}}^{(\text{SV,amp})}(N, P)} = \frac{\pi e}{6} \approx 1.53 \text{ dB}. \quad (100)$$

Fig. 19 shows the mutual information vs. $\text{SNR}^{(\text{amp})}$ for amplifier noise-limited SV detection, comparing the 3-D optimal, 3-D exponential, MB, and uniform distributions. The $(12 \times 12 \times 12)$ constellations are uniformly spaced in Stokes space and the input distributions and amplifier noise standard deviation σ_{amp} are optimized using the methods outlined in Section III-D.

The 3-D exponential distribution outperforms the 3-D MB distribution over the range of $\text{SNR}^{(\text{amp})}$ studied. This is consistent with (98), which suggests that at high $\text{SNR}^{(\text{amp})}$, where the exponential factor dominates, the input distribution should be exponentially distributed in $\|\mathbf{s}\|_2 = s_0$.

The 3-D optimal distribution outperforms the 3-D exponential, MB, and uniform distributions, as expected. The 3-D exponential distribution achieves a mutual information within 0.1 bits/symbol of the 3-D optimal distribution at $\text{SNR}^{(\text{amp})} = 21$ dB. The shaping gain of the 3-D optimal distribution over the uniform distribution is 1.49 dB at 6.58 bits/symbol. This is larger than the 1.105 dB observed in [35] owing to the larger constellation size used in Fig. 19. We note that the comparison of the 3-D optimal distribution and the uniform distribution in Fig. 19 is not directly comparable to the ultimate shaping

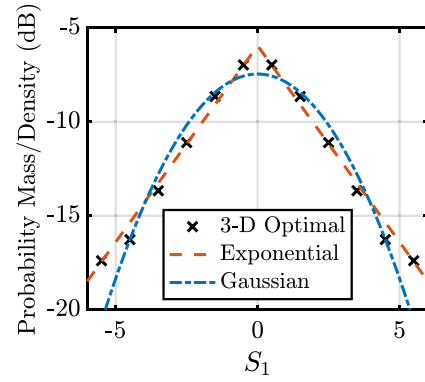


Fig. 20. 3-D optimal distribution vs. S_1 for $S_2 = S_3 = 0.5$ and $\text{SNR}^{(\text{amp})} = 25$ dB for amplifier noise-limited SV detection computed using the BA algorithm. The unnormalized continuous exponential and Gaussian densities are fitted to minimize the L_1 -norm of the fitting error in dB.

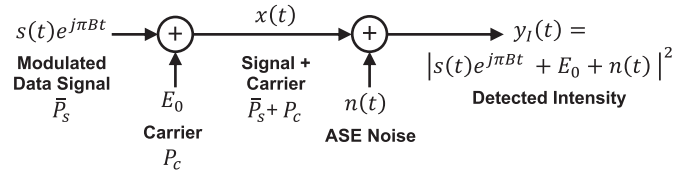


Fig. 21. Continuous-time channel model for KK detection in the amplifier noise-limited regime. The total transmitted signal power is equal to the sum of the modulated data signal power \bar{P}_s and the carrier power P_c . The detected intensity $y(t)$ is processed to recover the phase of the received electric field. Adapted from [45].

gain derived in (100). The uniform distribution in Stokes space presumed in Fig. 19 is not equivalent to the uniform distribution in scaled Stokes space used in the derivation of (100).

Fig. 20 shows the 3-D optimal distribution vs. S_1 for $S_2 = S_3 = 0.5$ and $\text{SNR}^{(\text{amp})} = 25$ dB computed using the BA algorithm. The continuous exponential and Gaussian distributions are optimized to minimize the L_1 -norm of the fitting error in dB. Similar to Fig. 16, the exponential distribution better fits the optimal PMF than the Gaussian distribution does. The exponential distribution still provides a reasonable fit in spite of neglecting the factor of $1/\|\mathbf{S}\|_2^{3/2}$ in (98). The L_1 -norm of the fitting error for the exponential distribution is lower in the thermal noise-limited regime (Fig. 16) than in the amplifier noise-limited regime (Fig. 20), presumably because of the neglect of the factor $1/\|\mathbf{S}\|_2^{3/2}$ in the latter regime.

F. Kramers Kronig Detection, Amplifier Noise-Limited

Kramers Kronig detection [25] enables coherent detection without requiring a LO laser at the receiver. Unlike the other DD-based methods discussed in the previous subsections, an approximately optimal input distribution can be obtained analytically using MMI [1], and application of HCA [31] is not strictly required. In this subsection, we mainly review the study of KK detection in the amplifier noise-limited regime presented in [27].

1) *Continuous-Time Channel Model:* Fig. 21 presents a continuous-time channel model for a KK receiver in the amplifier noise-limited regime. This continuous time model is adapted

from [27], which assumes that the unmodulated carrier is added at the transmitter. Centered at the frequency of the unmodulated carrier and using band-limited Nyquist pulses, the noiseless continuous-time transmitted signal is

$$x(t) = E_0 + s(t)e^{j\pi Bt}, \quad (101)$$

where E_0 is the unmodulated carrier, $s(t)$ is the information-bearing modulated signal, and B is the bandwidth of $s(t)$.

The transmitted signal (101) is minimum-phase provided the carrier power P_c is sufficient to ensure that time-domain trajectories of $x(t)$ do not encircle the origin. If the minimum-phase condition is satisfied, the phase $\varphi(t) = \arg\{x(t)\}$ can be obtained from the intensity $|x(t)|^2$ by using the Hilbert transform \mathcal{H} :

$$\varphi(t) = \mathcal{H}\{\log \sqrt{|x(t)|^2}\}. \quad (102)$$

Assuming ideal phase reconstruction of $\varphi(t)$, $s(t)$ can be obtained by

$$s(t) = \left(\sqrt{|x(t)|^2} e^{j\varphi(t)} - E_0 \right) e^{-j\pi Bt}. \quad (103)$$

Near-lossless implementations of (102) and (103) can be realized using samples of $|x(t)|^2$ with an oversampling ratio of 2 and digital signal processing [53].

Assuming transmission through a non-dispersive channel for simplicity, the detected electrical current in an amplifier noise-limited KK receiver is

$$y_I(t) = |x(t) + n(t)|^2, \quad (104)$$

where $n(t)$ is white complex Gaussian noise with one-sided PSD N_0 . The KK receiver subsequently computes the Hilbert transform of $\log \sqrt{y_I(t)}$. Phase-retrieval errors can occur if the noise causes time-domain trajectories of $x(t) + n(t)$ to encircle the origin, which would result in a recovered phase $\varphi(t)$ not equal to $\mathcal{H}\{\log \sqrt{|x(t) + n(t)|^2}\}$. For simplicity, we have assumed the signal and ASE noise are received in one polarization. This enables us to write the channel model (104) as a complex, scalar channel. KK detection of dual-polarization signals is possible in principle, but may be complicated in practice [27].

The channel model can be further simplified if we assume the carrier is sufficiently strong to ensure $x(t) + n(t)$ is minimum-phase, which we refer to as the high carrier-to-signal power (CSPR) regime. In this regime, assuming ideal phase reconstruction, the received electric field can be reconstructed exactly from the detected intensity as $x(t) + n(t) = \sqrt{y_I(t)} e^{j\mathcal{H}\{\log \sqrt{y_I(t)}\}}$, and we can employ an intermediate continuous-time channel for KK detection:

$$y(t) = x(t) + n(t) \quad (105)$$

$$= E_0 + s(t)e^{j\pi Bt} + n(t). \quad (106)$$

After subtracting the unmodulated carrier E_0 and multiplying by $e^{-j\pi Bt}$ to remove the frequency shift, the continuous-time channel model for KK detection in the high-CSPR regime becomes

$$\begin{aligned} y'(t) &= (y(t) - E_0) e^{-j\pi Bt} \\ &= s(t) + n'(t). \end{aligned} \quad (107)$$

The channel output (107) comprises the information-bearing modulated signal $s(t)$ plus $n'(t) = n(t)e^{-j\pi Bt}$, which is an additive white Gaussian noise with PSD N_0 .

2) *Channel Capacity and Optimal Input Distribution*: The total average transmit power is $P_c + \bar{P}_s$, the sum of the carrier power P_c and the modulated signal average power \bar{P}_s . The two powers are additive because the carrier and modulated signal do not overlap in frequency. The received SNR is defined as

$$\begin{aligned} \text{SNR}^{(\text{amp})} &= \frac{\bar{P}_s + P_c}{N_0 B} \\ &= \text{SNR}_{\text{sig}} (1 + \text{CSPR}), \end{aligned} \quad (108)$$

where $\text{SNR}_{\text{sig}} = \bar{P}_s / N_0 B$ is the SNR excluding the carrier and $\text{CSPR} = P_c / \bar{P}_s$ is the carrier-to-signal power ratio.

The general form for the capacity of the amplifier noise-limited KK receiver is the maximum mutual information between X and $y_I(t)$ from (104):

$$C^{(\text{KK})}(\text{SNR}^{(\text{amp})}) = \max_{\substack{P_c, f_S(s): \\ \mathbb{E}[|S|^2] \leq \bar{P}_s \\ P_c + \bar{P}_s \leq \text{SNR}^{(\text{amp})} N_0 B}} I(X; Y_I), \quad (109)$$

where $f_S(s)$ is the PDF of the modulated signal $s(t)$ and $\text{SNR}^{(\text{amp})}$ is the SNR constraint. Owing to the complexity of phase retrieval, the capacity of KK detection for arbitrary CSPR is an open problem.

A closed-form analytical expression for the capacity-achieving input distribution can be derived in the high-CSPR regime [27]. Assuming P_c is sufficient to ensure ideal phase recovery, there is a one-to-one relationship between $y(t)$ and $y_I(t)$, and we can equate $I(X; Y_I) = I(X; Y)$, where Y is a random variable for $y(t)$ in (105). The addition of a carrier or a frequency shift of $s(t)$ do not change mutual information, so we obtain $I(X; Y) = I(S; Y)$. For a given $\text{SNR}^{(\text{amp})}$, the power available for $s(t)$ is $\bar{P}_s \leq \text{SNR}^{(\text{amp})} N_0 B - P_c$. Using these observations, the optimization in (109) simplifies to

$$C^{(\text{KK,CSPR})}(\text{SNR}^{(\text{amp})}) = \max_{\substack{f_S(s): \\ \mathbb{E}[|S|^2] \leq \bar{P}_s \\ \bar{P}_s \leq \text{SNR}^{(\text{amp})} N_0 B - P_c}} I(S; Y), \quad (110)$$

where $C^{(\text{KK,CSPR})}$ indicates the capacity in the high-CSPR regime. Using the independence of the signal and noise, the optimization problem simplifies to maximizing $h(S) - h(N)$ subject to $\mathbb{E}[|S|^2] \leq \text{SNR}^{(\text{amp})} N_0 B - P_c$.

Using reasoning similar to that in Section III-A, the capacity-achieving input distribution for KK detection in the high-CSPR regime described by (110) is $S \sim \mathcal{CN}(0, \bar{P}_s)$, a 2-D complex circular Gaussian distribution with variance $\bar{P}_s = \text{SNR}^{(\text{amp})} N_0 B - P_c$. Using minimum-bandwidth Nyquist pulses and the capacity-achieving input distribution, the capacity of KK detection in the high-CSPR regime is

$$\begin{aligned} C^{(\text{KK,CSPR})}(\text{SNR}^{(\text{amp})}) &= B \log_2 (1 + \text{SNR}_{\text{sig}}) \\ &= B \log_2 \left(1 + \frac{\text{SNR}^{(\text{amp})}}{1 + \text{CSPR}} \right), \end{aligned} \quad (111)$$

achieving a spectral efficiency $\log_2(1 + \text{SNR}_{\text{sig}})$ bits/symbol.

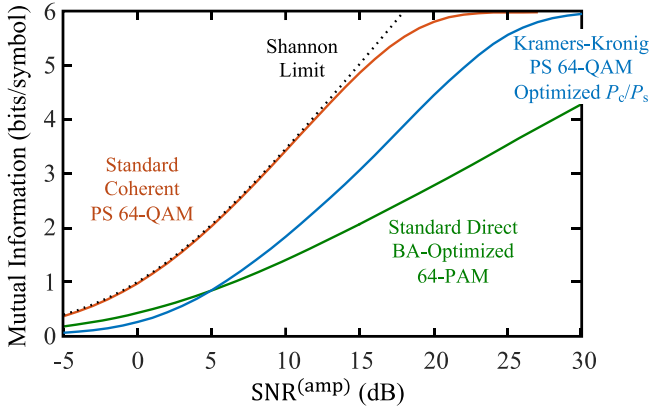


Fig. 22. Mutual information vs. $\text{SNR}^{(\text{amp})}$ for amplifier noise-limited SC detection, KK detection and SD detection, compared to the Shannon capacity for SC detection. For SC and KK detection, (8×8) constellations are shaped by MB distributions optimized at each $\text{SNR}^{(\text{amp})}$ (jointly optimized with the CSPR for KK detection). For SD detection, a 64-point constellation is optimized at each $\text{SNR}^{(\text{amp})}$ using the BA algorithm. Adapted from [27].

3) *High-Rate Continuous Approximation:* In the high-CSPR regime, the general KK receiver continuous-time channel in (104) can be transformed to the AWGN channel in (107). Symbol-rate sampling yields a sufficient statistic, leading to a discrete-time channel model

$$y'[n] = s[n] + n'[n]. \quad (112)$$

The discrete-time channel model is equivalent to the SC channel model given in (1), except for the implicit transmitted carrier. Therefore, the HCA derivation for the amplifier noise-limited KK detection in the high-CSPR regime is very similar to that for SC detection. For sake of brevity, we omit the derivation and summarize the results in Table II, which is explained in Section IV-G.

4) *Numerical Analysis:* While analytical solution of (109) is an open problem, the mutual information achieved by KK detection can be estimated numerically using methods presented in Section III-D. Fig. 22 shows the mutual information vs. $\text{SNR}^{(\text{amp})}$ for SC detection, KK detection, and SD detection, comparing them to the Shannon capacity (4). For SC and KK detection, (8×8) uniformly spaced constellations are shaped by MB distributions optimized at each $\text{SNR}^{(\text{amp})}$ (jointly optimized with the CSPR for KK detection). For SD detection, a 64-point uniformly spaced constellation is optimized at each $\text{SNR}^{(\text{amp})}$ using the BA algorithm.

In Fig. 22, comparing KK and SC detection, we observe that KK detection incurs a penalty of 5–7dB compared to SC detection in terms of the $\text{SNR}^{(\text{amp})}$ required to achieve a given mutual information over the range of SNRs studied. This SNR penalty corresponds to the power used in the unmodulated carrier. Ignoring the effect of limited constellation size near 6 bits/symbol, the gap between the SC and KK receivers grows monotonically with increasing $\text{SNR}^{(\text{amp})}$. Although KK detection nominally provides 2 real dimensions per polarization, the effective degrees of freedom are only about 1.8, because as $\text{SNR}^{(\text{amp})}$ increases, it is necessary to continuously increase CSPR to ensure ever-more-accurate phase retrieval [27].

Comparing KK and SD detection in Fig. 22, we observe that KK detection significantly outperforms SD detection at high $\text{SNR}^{(\text{amp})}$, owing to its advantage in degrees of freedom (about 1.8 for KK detection vs. 1 for SD detection). Interestingly, however, SD detection outperforms KK detection for $\text{SNR}^{(\text{amp})} < 5\text{dB}$. At these very low SNRs, the optimal input distribution for SD detection has a high probability at the zero intensity level, which has the lowest noise. By contrast, for KK detection, the need to satisfy a minimum-phase requirement prevents the use of the zero intensity level, tending to increase the noise detected at the receiver.

G. Summary of Shaping Results

Table II summarizes the optimal shaping regions, induced distributions on the constituent constellation, and ultimate shaping gains for the six discrete-time channels considered in this paper. We observe several interesting similarities when comparing the shaping regions and induced distributions in this common framework.

The optimal shaping region for thermal noise-limited SD detection and SV detection are both N -simplexes in signal intensity. The induced distribution for SD detection is an exponential distribution in the intensity. For SV detection, the induced distribution is an exponential distribution in the intensity S_0 . Because the intensity S_0 is an L_2 -norm of the Stokes parameters $\{S_1, S_2, S_3\}$, the induced distribution is a 3-D exponential distribution in the Stokes parameters.

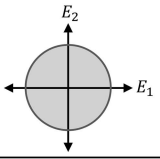
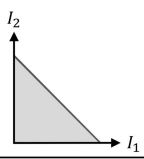
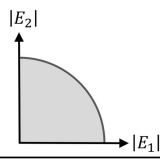
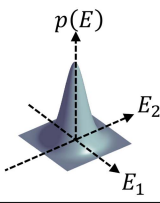
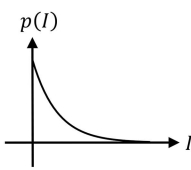
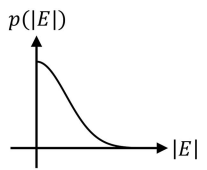
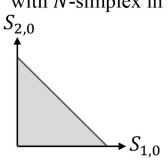
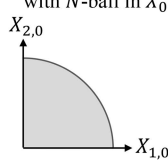
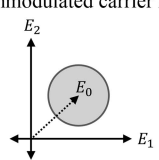
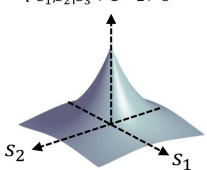
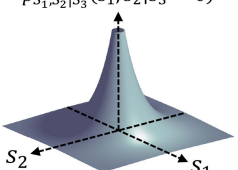
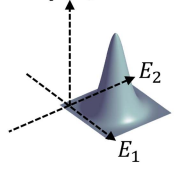
The optimal shaping regions for amplifier noise-limited SD detection and SV detection are nonnegative orthants intersected with N -balls in $|E|$ and X_0 , respectively. These induce, respectively, N -D and $3N$ -D balls in the natural coordinates. The induced distribution for SD detection is a half-Gaussian distribution in electric field magnitude $|E|$, which corresponds to a Gamma distribution with shape parameter $1/2$ in the intensity. The induced distribution for SV detection is a Gamma distribution with shape parameter $3/2$ in the intensity. We observe that the induced intensity distributions for amplifier noise-limited SD detection and SV detection are Gamma distributions with shape parameters equal to half the number of signaling dimensions.

The optimal shaping regions for SC detection and amplifier noise-limited KK detection are both hyperballs in electric field with radii equal to the square root of the respective peak constraints on the total signal power. The shaping region for the SC receiver is centered at the origin while the shaping region for the SC receiver is centered at the unmodulated carrier E_0 , which is required to ensure the received signal is minimum-phase. The induced distributions are both complex circular Gaussian, which are centered at the origin and at E_0 , respectively.

V. IMPLEMENTATION OF PROBABILISTIC SHAPING

While HCA provides analytical continuous approximations to the optimal input distributions, at least at high SNR, discrete constellations with a finite number of signal points must be used in practice. Hence, some means of obtaining an optimized discrete input distribution must be used. Methods commonly

TABLE II
 SUMMARY OF SHAPING RESULTS FOR SIX CHANNEL MODELS IN OPTICAL COMMUNICATIONS

Detection Method & Dominant Noise	Standard coherent detection, amplifier or LO shot noise	Standard direct detection, thermal noise	Standard direct detection, amplifier noise
Natural Coordinates	1-D complex electric field $E = E_1 + jE_2$	1-D electric field intensity $I = E ^2$	1-D electric field magnitude $ E $
Optimal Shaping Region	N -D complex ball centered at the origin 	Nonnegative orthant intersected with N -simplex 	Nonnegative orthant intersected with N -ball 
Induced Marginal Density in the Constituent Constellation	$p(E) = \frac{1}{\pi\bar{P}} \exp\left(-\frac{ E ^2}{\bar{P}}\right)$, $E = E_1 + jE_2$ 	$p(I) = \frac{1}{\bar{P}} \exp\left(-\frac{I}{\bar{P}}\right)$, $I \geq 0$ 	$p(E) = \sqrt{\frac{2}{\pi\bar{P}}} \exp\left(-\frac{ E ^2}{2\bar{P}}\right)$, $ E \geq 0$ 
Ultimate Shaping Gain	$\pi e/6 \approx 1.53$ dB	$e/2 \approx 1.33$ dB	$\pi e/6 \approx 1.53$ dB
Induced Distribution	Complex circular Gaussian	Exponential	Half-Gaussian
Key Works	[31], [46], [47], [54]	[32], [33]	[34]
Detection Method & Dominant Noise	Stokes vector detection, thermal noise	Stokes vector detection, amplifier noise	Kramers Kronig detection, amplifier noise
Natural Coordinates	3-D Stokes vector $\mathbf{S} = \{S_1, S_2, S_3\}$	3-D scaled Stokes vector $\mathbf{X} = \{X_1, X_2, X_3\} = \{S_1, S_2, S_3\}/\sqrt{S_0}$	1-D complex electric field $E = E_1 + jE_2$
Optimal Shaping Region	Nonnegative orthant intersected with N -simplex in S_0 	Nonnegative orthant intersected with N -ball in X_0 	N -D complex ball centered at the unmodulated carrier E_0 
Induced Marginal Density in the Constituent Constellation	$p(\mathbf{S}) = \frac{1}{8\pi} \frac{1}{(\bar{P}/3)^3} \exp\left(-\frac{\ \mathbf{S}\ _2}{\bar{P}/3}\right)$, $\mathbf{S} = (S_1, S_2, S_3)$ $p_{S_1, S_2 S_3}(S_1, S_2 S_3 = 0)$ 	$p(\mathbf{S}) = \frac{1}{2} \left(\frac{1}{2\pi\ \mathbf{S}\ _2(\bar{P}/3)}\right)^{3/2} \exp\left(-\frac{1}{2} \frac{\ \mathbf{S}\ _2}{\bar{P}/3}\right)$, $\mathbf{S} = (S_1, S_2, S_3)$ $p_{S_1, S_2 S_3}(S_1, S_2 S_3 = 0)$ 	$p(E) = \frac{1}{\pi\bar{P}_s} \exp\left(-\frac{ E - E_0 ^2}{\bar{P}_s}\right)$, $E = E_1 + jE_2$ 
Ultimate Shaping Gain	$\sim 0.961^3 \sqrt{\pi e}/3 \approx 1.056$ dB	$\pi e/6 \approx 1.53$ dB	$\leq \pi e/6 \approx 1.53$ dB
Induced Distribution	3-D exponential	Gamma with shape parameter 3/2	Shifted complex circular Gaussian
Key Works	[35]	[35]	[27]

employed include the BA algorithm and sampling and normalizing a continuous input distribution. We refer the reader to Section III-D for an overview of these methods.

In the remainder of this section, we consider other important aspects of implementing coded modulation with probabilistic shaping, emphasizing certain issues that arise with DD-based detection methods but not typically with SC detection. We first review DM and the PAS architecture to identify restrictions on the output distribution imposed by PAS. We then study how the separability and symmetry of the continuous input distributions derived for DD-based methods affect the implementation and performance of probabilistic shaping.

A. Conventional Implementation of Discrete Input Distributions

A conventional approach to achieving a target nonuniform discrete input distribution is to combine an FEC code and a DM using the PAS architecture [5], [36]. A DM is an algorithm that maps uniform input bits to a sequence of symbols whose empirical distribution closely follows a target discrete distribution. CCDM and sphere shaping are two important classes of DM methods that have been studied extensively for optical communications [4], [5]. CCDM maps uniform input bits to symbol sequences whose empirical distribution exactly equals a target distribution. The constant-composition property can be exploited to enable a fixed-length-to-fixed-length implementation using simple arithmetic coding [3]. By contrast, sphere shaping maps uniform input bit sequences to symbol sequences that satisfy a maximum-energy constraint [4]. While both CCDM and sphere shaping are capacity-achieving in the limit of an infinite-length DM, sphere shaping exhibits performance superior to CCDM at finite block lengths.

PAS is a layered architecture that enables the integration of DM with an existing FEC code [2], [5]. The PAS architecture requires that the target probability distribution have probability masses that occur in equal-probability pairs. Using this structure, the symbol sequence output by the DM can be uniquely mapped to a pair of symbols with equal probabilities. A combination of bits output by the FEC code and additional information bits are used to uniformly choose among pairs of symbols with equal probabilities. We use the term *pairwise symmetry* to denote continuous or discrete probability distributions in which the probability masses or densities occur in equal-probability pairs.

The MB distribution is a near-capacity-achieving input distribution for the SC channel obtained by sampling and normalizing a continuous Gaussian distribution [46]. There are conditions on the constellation points at which the continuous Gaussian distribution is sampled to ensure the resulting MB distribution is both separable and has pairwise symmetry.

Separability of a multi-variate distribution refers to its ability to be expressed as a product of distributions for the individual variables. An N -D MB distribution is separable into the product of N identically distributed 1-D MB distributions provided the sampling constellation is described as the N -fold Cartesian product of a 1-D constellation [46]. In the remainder of Section V, we assume that a continuous distribution is sampled using

TABLE III
CATEGORIZATION OF OPTIMAL INPUT DISTRIBUTIONS FOR FIVE DIRECT DETECTION-BASED CHANNEL MODELS

	Losslessly Separable into 1-D Distributions	Not Losslessly Separable into 1-D Distributions
Symmetric Distribution	KK amplifier (shifted Gaussian)	SV thermal (3-D exponential) SV amplifier (Gamma, shape parameter 3/2)
Asymmetric Distribution	SD thermal (1-D exponential) SD amplifier (1-D half-Gaussian)	

KK: Kramers Kronig, SD: standard direct, SV: Stokes vector.

a constellation formed by the N -fold Cartesian product of a 1-D constellation. The pairwise symmetry of the MB distribution is guaranteed provided the sampling constellation has bipolar symmetry. In the remainder of Section V, we assume that when the underlying continuous distribution has bipolar symmetry, the sampling constellation has bipolar symmetry.

The optimal continuous input distribution for SC detection is a complex circular Gaussian distribution (we consider one polarization for simplicity). This is equivalent to a 2-D real IID Gaussian distribution. This distribution is symmetric and has bipolar symmetry and can therefore be implemented using two independent 1-D PAS encoders.

B. Implementation of Shaping With Direct Detection

Table III categorizes the optimal input distributions for amplifier noise-limited KK detection, thermal noise-limited and amplifier noise-limited SD detection, and thermal noise-limited and amplifier noise-limited SV detection based on bipolar symmetry and separability.

For amplifier noise-limited KK detection, the optimal input distribution has bipolar symmetry about the transmitted carrier and is separable into independent 1-D distributions. This enables lossless implementation by independent 1-D PAS encoders.

For SD detection in both noise regimes, the optimal input distributions are asymmetric, which precludes straightforward implementation using PAS. The distributions are unipolar and monotonically decreasing, so there is no sampling constellation that can achieve pairwise symmetry in the resulting discrete distribution. Two common approaches to overcoming this lack of pairwise symmetry include modifying the input distribution to have pairwise symmetry, which results in a small loss in achievable rate, or using a non-PAS scheme [5], [55], [56].

For SV detection in the thermal and amplifier noise-limited regimes, the optimal input distributions are 3-D exponential and Gamma with shape parameter 3/2, respectively. These can be sampled by a constellation with bipolar symmetry to yield 3-D discrete distributions, which can be implemented by 3-D PAS encoders. The two 3-D discrete distributions are not losslessly separable into products of 1-D distributions, owing to the L_2 -norms appearing in the expressions. Nevertheless, each 3-D discrete distribution can be approximated by a product of 1-D distributions with a small loss in achievable rate [35].

VI. CONCLUSION

In this tutorial, we presented a comprehensive overview of probabilistic shaping in DD-based optical communication systems. We reviewed DD-based detection methods and presented discrete-time channel models for thermal noise-limited and amplifier noise-limited SD detection and SV detection, and amplifier noise-limited KK detection. Exploiting the concept of natural coordinates, we used HCA to compute continuous analytical approximations to the optimal input distributions and the shaping gains for SD detection and SV detection in the thermal noise-limited and amplifier noise-limited regimes. We also studied the optimal input distribution and achievable rate for amplifier noise-limited KK detection in the high-CSPR regime using both MMI and HCA. We discussed some considerations in algorithmic implementation of probabilistic shaping in DD-based systems based on the separability and symmetry of the optimal input distributions.

ACKNOWLEDGMENT

The authors are grateful for the thoughtful suggestions of the reviewers, which helped them improve this paper substantially. Any opinions, findings, and conclusions or recommendations expressed here are those of the authors and do not necessarily reflect the views of the National Science Foundation.

REFERENCES

- [1] C. E. Shannon, "A mathematical theory of communication," *Bell Syst. Tech. J.*, vol. 27, no. 3, pp. 379–423, 1948.
- [2] G. Böcherer, F. Steiner, and P. Schulte, "Bandwidth efficient and rate-matched low-density parity-check coded modulation," *IEEE Trans. Commun.*, vol. 63, no. 12, pp. 4651–4665, Dec. 2015.
- [3] P. Schulte and G. Böcherer, "Constant composition distribution matching," *IEEE Trans. Inf. Theory*, vol. 62, no. 1, pp. 430–434, Jan. 2016.
- [4] A. Amari et al., "Introducing enumerative sphere shaping for optical communication systems with short blocklengths," *J. Lightw. Technol.*, vol. 37, no. 23, pp. 5926–5936, Dec. 2019.
- [5] G. Böcherer, P. Schulte, and F. Steiner, "Probabilistic shaping and forward error correction for fiber-optic communication systems," *J. Lightw. Technol.*, vol. 37, no. 2, pp. 230–244, Jan. 2019.
- [6] A. Goldsmith, *Wireless Communications*. New York, NY, USA: Cambridge Univ. Press, 2005.
- [7] E. Telatar, "Capacity of multi-antenna Gaussian channels," *Eur. Trans. Telecommun.*, vol. 10, no. 6, pp. 585–595, 1999.
- [8] A. Goldsmith, S. A. Jafar, N. Jindal, and S. Vishwanath, "Capacity limits of MIMO channels," *IEEE J. Sel. Areas Commun.*, vol. 21, no. 5, pp. 684–702, Jun. 2003.
- [9] R. Gallager, "A perspective on multiaccess channels," *IEEE Trans. Inf. Theory*, vol. 31, no. 2, pp. 124–142, Mar. 1985.
- [10] H. Liao, "Multiple access channels," Ph.D. dissertation, Univ. Hawaii, 1972.
- [11] R. Blahut, "Computation of channel capacity and rate-distortion functions," *IEEE Trans. Inf. Theory*, vol. 18, no. 4, pp. 460–473, Jul. 1972.
- [12] S. Arimoto, "An algorithm for computing the capacity of arbitrary discrete memoryless channels," *IEEE Trans. Inf. Theory*, vol. 18, no. 1, pp. 14–20, Jan. 1972.
- [13] A. Chaaban and S. Hranilovic, "Capacity of optical wireless communication channels," *Philos. Trans. Roy. Soc. A*, vol. 378, no. 2169, 2020, Art. no. 20190184.
- [14] A. Chaaban, Z. Rezeki, and M.-S. Alouini, "On the capacity of intensity-modulation direct-detection Gaussian optical wireless communication channels: A tutorial," *IEEE Commun. Surv. Tut.*, vol. 24, no. 1, pp. 455–491, Firstquarter 2022.
- [15] S. Hranilovic and F. Kschischang, "Capacity bounds for power- and band-limited optical intensity channels corrupted by Gaussian noise," *IEEE Trans. Inf. Theory*, vol. 50, no. 5, pp. 784–795, May 2004.
- [16] A. A. Farid and S. Hranilovic, "Capacity bounds for wireless optical intensity channels with Gaussian noise," *IEEE Trans. Inf. Theory*, vol. 56, no. 12, pp. 6066–6077, Dec. 2010.
- [17] A. Lapidath, S. M. Moser, and M. A. Wigger, "On the capacity of free-space optical intensity channels," *IEEE Trans. Inf. Theory*, vol. 55, no. 10, pp. 4449–4461, Oct. 2009.
- [18] A. A. Farid and S. Hranilovic, "Channel capacity and non-uniform signalling for free-space optical intensity channels," *IEEE J. Sel. Areas Commun.*, vol. 27, no. 9, pp. 1553–1563, Dec. 2009.
- [19] S. M. Moser, "Capacity results of an optical intensity channel with input-dependent Gaussian noise," *IEEE Trans. Inf. Theory*, vol. 58, no. 1, pp. 207–223, Jan. 2012.
- [20] T. H. Chan, S. Hranilovic, and F. Kschischang, "Capacity-achieving probability measure for conditionally Gaussian channels with bounded inputs," *IEEE Trans. Inf. Theory*, vol. 51, no. 6, pp. 2073–2088, Jun. 2005.
- [21] M. Soltani and Z. Rezeki, "Results on the rate-equivocation region of the degraded signal-dependent noise wiretap channel," *IEEE Commun. Lett.*, vol. 24, no. 9, pp. 1914–1918, Sep. 2020.
- [22] E. Ip, A. P. T. Lau, D. J. Barros, and J. M. Kahn, "Coherent detection in optical fiber systems," *Opt. Exp.*, vol. 16, no. 2, pp. 753–791, 2008.
- [23] D. Che, A. Li, X. Chen, Q. Hu, Y. Wang, and W. Shieh, "Stokes vector direct detection for short-reach optical communication," *Opt. Lett.*, vol. 39, no. 11, pp. 3110–3113, Jun. 2014.
- [24] W. Shieh, H. Khodakarami, and D. Che, "Invited article: Polarization diversity and modulation for high-speed optical communications: Architectures and capacity," *APL Photon.*, vol. 1, no. 4, 2016, Art. no. 040801.
- [25] A. Mecozzi, C. Antonelli, and M. Shtaif, "Kramers–Kronig coherent receiver," *Optica*, vol. 3, no. 11, pp. 1220–1227, Nov. 2016.
- [26] H. Khodakarami, D. Che, and W. Shieh, "Information capacity of polarization-modulated and directly detected optical systems dominated by amplified spontaneous emission noise," *J. Lightw. Technol.*, vol. 35, no. 14, pp. 2797–2802, Jul. 2017.
- [27] E. S. Chou, H. Srinivas, and J. M. Kahn, "Phase retrieval-based coherent receivers: Signal design and degrees of freedom," *J. Lightw. Technol.*, vol. 40, no. 5, pp. 1296–1307, Mar. 2022.
- [28] W. R. Bennett, "Spectra of quantized signals," *Bell Syst. Tech. J.*, vol. 27, no. 3, pp. 446–472, 1948.
- [29] A. Gersho, "Asymptotically optimal block quantization," *IEEE Trans. Inf. Theory*, vol. 25, no. 4, pp. 373–380, Jun. 1979.
- [30] T. Lookabaugh and R. Gray, "High-resolution quantization theory and the vector quantizer advantage," *IEEE Trans. Inf. Theory*, vol. 35, no. 5, pp. 1020–1033, Sep. 1989.
- [31] G. D. Forney and L.-F. Wei, "Multidimensional constellations. I. Introduction, figures of merit, and generalized cross constellations," *IEEE J. Sel. Areas Commun.*, vol. 7, no. 6, pp. 877–892, Aug. 1989.
- [32] D.-S. Shiu and J. M. Kahn, "Shaping and nonequiprobable signaling for intensity-modulated signals," *IEEE Trans. Inf. Theory*, vol. 45, no. 7, pp. 2661–2668, Nov. 1999.
- [33] S. Hranilovic and F. Kschischang, "Optical intensity-modulated direct detection channels: Signal space and lattice codes," *IEEE Trans. Inf. Theory*, vol. 49, no. 6, pp. 1385–1399, Jun. 2003.
- [34] W. Mao and J. M. Kahn, "Lattice codes for amplified direct-detection optical systems," *IEEE Trans. Commun.*, vol. 56, no. 7, pp. 1137–1145, Jul. 2008.
- [35] H. Jia, E. Liang, and J. M. Kahn, "Optimal shaping for the Stokes vector receiver," *J. Lightw. Technol.*, vol. 41, no. 22, pp. 6884–6897, Nov. 2023.
- [36] J. Cho and P. J. Winzer, "Probabilistic constellation shaping for optical fiber communications," *J. Lightw. Technol.*, vol. 37, no. 6, pp. 1590–1607, Mar. 2019.
- [37] J. Cho, "Probabilistic constellation shaping: An implementation perspective," in *Proc. 2022 Opt. Fiber Commun. Conf. Exhib.*, 2022, pp. 1–39.
- [38] D. Che, J. Cho, and X. Chen, "Does probabilistic constellation shaping benefit IM-DD systems without optical amplifiers?," *J. Lightw. Technol.*, vol. 39, no. 15, pp. 4997–5007, Aug. 2021.
- [39] M. Morsy-Osman, M. Chagnon, and D. V. Plant, "Four-dimensional modulation and Stokes direct detection of polarization division multiplexed intensities, inter polarization phase and inter polarization differential phase," *J. Lightw. Technol.*, vol. 34, no. 7, pp. 1585–1592, Apr. 2016.
- [40] M. Jean, K. Schulmeister, D. J. Lund, and B. E. Stuck, "Laser-induced corneal injury: Validation of a computer model to predict thresholds," *Biomed. Opt. Exp.*, vol. 12, no. 1, pp. 336–353, Jan. 2021.
- [41] J. Kahn and J. Barry, "Wireless infrared communications," *Proc. IEEE*, vol. 85, no. 2, pp. 265–298, Feb. 1997.
- [42] H. Srinivas et al., "Modeling and experimental measurement of power efficiency for power-limited SDM submarine transmission systems," *J. Lightw. Technol.*, vol. 39, no. 8, pp. 2376–2386, Apr. 2021.

- [43] T. Wiegart, F. D. Ros, M. P. Yankov, F. Steiner, S. Gaiarin, and R. D. Wesel, "Probabilistically shaped 4-PAM for short-reach IM/DD links with a peak power constraint," *J. Lightw. Technol.*, vol. 39, no. 2, pp. 400–405, Jan. 2021.
- [44] S. Hranilovic, "Minimum-bandwidth optical intensity Nyquist pulses," *IEEE Trans. Commun.*, vol. 55, no. 3, pp. 574–583, Mar. 2007.
- [45] J. M. Kahn and E. M. Liang, "Probabilistic shaping for direct-detection optical systems," in *Proc. Opt. Fiber Commun. Conf.*, Optica Publishing Group, 2024, p. M2B-1.
- [46] F. R. Kschischang and S. Pasupathy, "Optimal nonuniform signaling for Gaussian channels," *IEEE Trans. Inf. Theory*, vol. 39, no. 3, pp. 913–929, May 1993.
- [47] A. Calderbank and L. Ozarow, "Nonequiprobable signaling on the Gaussian channel," *IEEE Trans. Inf. Theory*, vol. 36, no. 4, pp. 726–740, Jul. 1990.
- [48] T. M. Cover and J. A. Thomas, *Elements of Information Theory*. Hoboken, NJ, USA: Wiley, 2006.
- [49] G. Böcherer, "Probabilistic signal shaping for bit-metric decoding," in *Proc. 2014 IEEE Int. Symp. Inf. Theory*, 2014, pp. 431–435.
- [50] T. Fehenberger, F. Kristl, C. Behrens, A. Ehrhardt, A. Gladisch, and N. Hanik, "Estimates of constrained coded modulation capacity for optical networks," in *Proc. Photonic Netw.; 15. ITG Symp.*, 2014, pp. 1–6.
- [51] S. N. Savenkov, *Jones and Mueller Matrices: Structure, Symmetry Relations and Information Content*. Berlin, Germany: Springer, 2009.
- [52] J. Proakis and M. Salehi, *Digital Communications*, 5th ed. New York, NY, USA: McGraw-Hill Higher Educ., 2008. [Online]. Available: <https://books.google.com/books?id=tOpKAQAACAAJ>
- [53] A. Mecozzi, C. Antonelli, and M. Shtaif, "Kramers–Kronig receivers," *Adv. Opt. Photon.*, vol. 11, no. 3, pp. 480–517, Sep. 2019.
- [54] V. Tarokh, A. Vardy, and K. Zeger, "Universal bound on the performance of lattice codes," *IEEE Trans. Inf. Theory*, vol. 45, no. 2, pp. 670–681, Mar. 1999.
- [55] Z. He, T. Bo, and H. Kim, "Probabilistically shaped coded modulation for IM/DD system," *Opt. Exp.*, vol. 27, no. 9, pp. 12126–12136, Apr. 2019.
- [56] T. Wiegart, L. Wang, D. Lentner, and R. D. Wesel, "Probabilistic shaping for asymmetric channels and low-density parity-check codes," in *Proc. 2023 12th Int. Symp. Topics Coding*, 2023, pp. 1–5.

Ethan M. Liang (Graduate Student Member, IEEE) received the A.S. degree in computer science from El Camino College, Torrance, CA, USA, in 2016, the B.S. degree in electrical engineering from the University of California at Los Angeles (UCLA), Los Angeles, CA, in 2019, and the M.S. degree in electrical engineering from Stanford University, Stanford, CA, in 2022. He is currently working toward the Ph.D. degree with the Department of Electrical Engineering, Stanford University. He is currently a National Science Foundation Graduate Research Fellow. His research interests include optical communications and coding theory.

Joseph M. Kahn (Life Fellow, IEEE) received the A.B., M.A., and Ph.D. degrees in physics from the University of California, Berkeley, CA, USA, in 1981, 1983, and 1986, respectively. In 1987–1990, he was with AT&T Bell Laboratories. In 1989, he demonstrated the first successful synchronous (i.e., coherent) detection using semiconductor lasers, achieving record receiver sensitivity. In 1990–2003, he was with the Electrical Engineering and Computer Sciences faculty at Berkeley. He demonstrated coherent detection of QPSK in 1992. In 1999, he with D. S. Shiu published the first work on probabilistic shaping for optical communications. In the 1990s and early 2000s, with his collaborators, he performed seminal work on indoor and outdoor free-space optical communications and multi-input multi-output wireless communications. In 2000, he with K. P. Ho founded StrataLight Communications, whose 40Gb/s-per-wavelength long-haul fiber transmission systems were deployed widely by AT&T, Deutsche Telekom, and other carriers. In 2002, Ho and Kahn applied to patent the first electronic compensation of fiber Kerr nonlinearity. StrataLight was acquired by Opnext in 2009. In 2003, he became the Professor of Electrical Engineering in the E. L. Ginzton Laboratory, Stanford University. He with his collaborators have extensively studied rate-adaptive coding and modulation, as well as digital signal processing for mitigating linear and nonlinear impairments in coherent systems. In 2008, he with E. Ip (and G. Li independently) invented simplified digital backpropagation for compensating fiber Kerr nonlinearity and dispersion. Since 2004, he with his collaborators have studied propagation, modal statistics, spatial multiplexing and imaging in multimode fibers, elucidating principal modes, and demonstrating transmission beyond the traditional bandwidth-distance limit in 2005, deriving the statistics of coupled modal group delays and gains in 2011, and deriving resolution limits for imaging in 2013. His research interests include optical frequency comb generators, coherent data center links, rate-adaptive access networks, fiber Kerr nonlinearity mitigation, ultra-long-haul submarine links, and optimal free-space transmission through atmospheric turbulence. He was the recipient of the National Science Foundation Presidential Young Investigator Award in 1991. In 2000, he became a Fellow of the IEEE.